

**CASTING AND SOLIDIFICATION TECHNOLOGY (CAST)
IML-1 FLIGHT EXPERIMENT**

**The University of Tennessee Space Institute
Center for Laser Applications
Tullahoma, TN 37388-8897**

December 1995

TABLE OF CONTENTS

I. INTRODUCTION	1
Objectives	1
II. CAST GROUND BASED EXPERIMENT DESCRIPTION	1
NH ₄ Cl-H ₂ O System	1
Ground-Based Solidification System	3
Ground-Based Experimental Optical Methods	4
Particle Tracking	4
Confocal Optical Signal Processing	4
Holographic Reconstruction	8
Image Analysis	9
CAST Fluids Thermal Model (FTM)	15
Numerical Model	15
Code Validation	16
Sensitivity Studies	20
CAST Linear Stability Model (LSM)	24
Numerical Model	26
III. CAST GROUND BASED EXPERIMENT RESULTS	28
IV. CAST IML-1 EXPERIMENT DESCRIPTION	36
Experimental Procedure	36
V. CAST FLIGHT EXPERIMENT RESULTS	38
Growth Rate Effects	38
Permeability Effects	39
Diffusion Layer Effects	40
Arm Spacing Effects	43
Computational Model Results	49
VI. CONCLUSIONS	60
VII. PI TEAM	62
VIII. REFERENCES	63
TABLES	
TABLE 1	3
TABLE 2	6
TABLE 3	20
TABLE 4	47
TABLE 5	49
APPENDIX: NOMENCLATURE	65

1.0 Executive Summary

NASA uses the Variable Polarity Plasma Arc Welding (VPPAW) process extensively for fabrication of Space Shuttle External Tanks. This welding process has been in use at NASA since the late 1970's, but the physics of the process has never been satisfactorily modeled and understood. In an attempt to advance the level of understanding of VPPAW, Dr. Arthur C. Nunes, Jr., (NASA) has developed a mathematical model of the process. The work described in this report evaluated and used two versions (level-1 level-2) of Dr. Nunes' model , and a model derived by the University of Alabama in Huntsville (UAH) from Dr. Nunes' level-1 model.

Two series of VPPAW experiments were done, using over 400 different combinations of welding parameters under contract NAS8-38812. Additional experiments were performed under this contract to expand the database. Observations were made of VPPAW process behavior as a function of specific welding parameter changes. Data from these weld experiments was used to evaluate and suggest improvements to Dr. Nunes' model.

Experimental data and correlations with the model were used to develop a multi-variable control algorithm for use with a future VPPAW controller. This algorithm is designed to control weld widths (both on crown and root of the weld) based upon the weld parameters, base metal properties, and real-time observation of the crown width. The algorithm exhibited accuracy comparable to that of the weld width measurements for both aluminum and mild steel welds.

CASTING AND SOLIDIFICATION TECHNOLOGY (CAST)

IML-1 FLIGHT EXPERIMENT

I. Introduction

Over the past four decades solidification theories concerning morphological instabilities¹⁻⁴ and constituent macrosegregation⁵⁻¹⁰ have been gradually maturing. The application of stability analyses has led to a greater appreciation for the parameters controlling the shape of the solid-liquid interface, and advanced Computational Fluid Dynamics (CFD) techniques have enabled researchers to investigate the relationship between mushy zone flow and macrosegregation. These analyses have indicated the significant influence of convection and, in this respect, point to microgravity as a potential solution for segregation and macrosegregation problems. Interestingly, however, the theories^{3,11,12} predict that buoyancy driven convective effects may still be present in microgravity.

The scale of convective effects that occur during dendritic solidification ranges from microscopic at the dendrite tips and arms, to macroscopic within the bulk fluid. Historically, convective behavior in such a solidifying dendritic system has received much less attention than it has for the planar case and the micro-scale convective regimes of the mushy zone and the diffusion layer are not yet adequately characterized. The relative roles of the macro and micro effects and how this relationship changes with gravity level has also not been defined.

Objectives

The objective of the CAST experiment was to perform a detailed characterization of the effects of convection on the governing growth parameters for unidirectional dendritic solidification. It accomplished this by 1) Developing a unified model of dendritic growth during controlled directional solidification, 2) Measuring minimally disturbed (micro-g) solutal and thermal fields for verification of the model components, and 3) Conducting convection-affected (one-g) directional solidification experiments for final verification.

II. CAST Ground Based Experiment Description

NH₄Cl-H₂O System

The NH₄Cl-H₂O system was used exclusively for the CAST experiments. It is a transparent metal-model that has a eutectic point and a high entropy of fusion and freezes dendritically similar to metal alloys. The significant properties necessary for computational modelling and optical diagnostics are either well known or have been determined by the authors. Additional characteristics pertinent for this study were: a low (room temperature) melting point, the solute (water) is less dense than the solvent (similar to superalloys), and its index of refraction is a strong linear function of both concentration

and temperature. The low density of the solute qualifies this system as a light solute rejecting alloy with the associated density inversion in the liquid due to the inverted density layer in the mushy zone (Figure 1a).

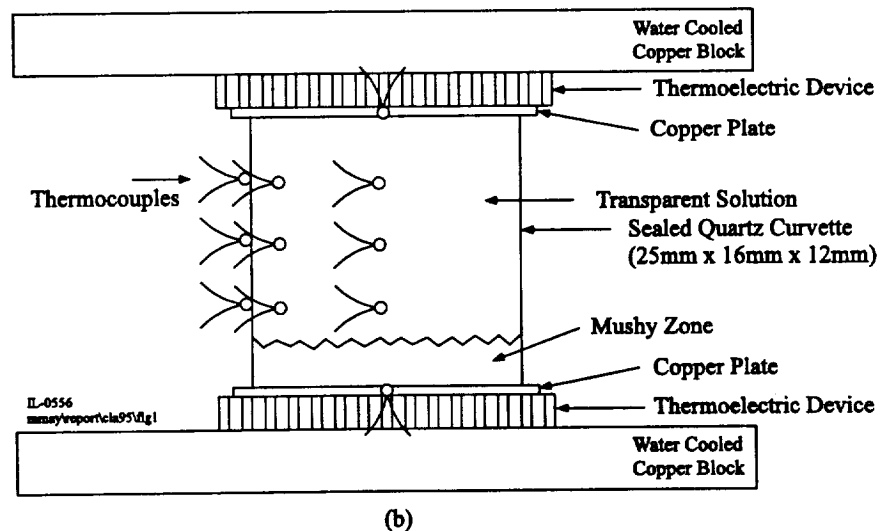
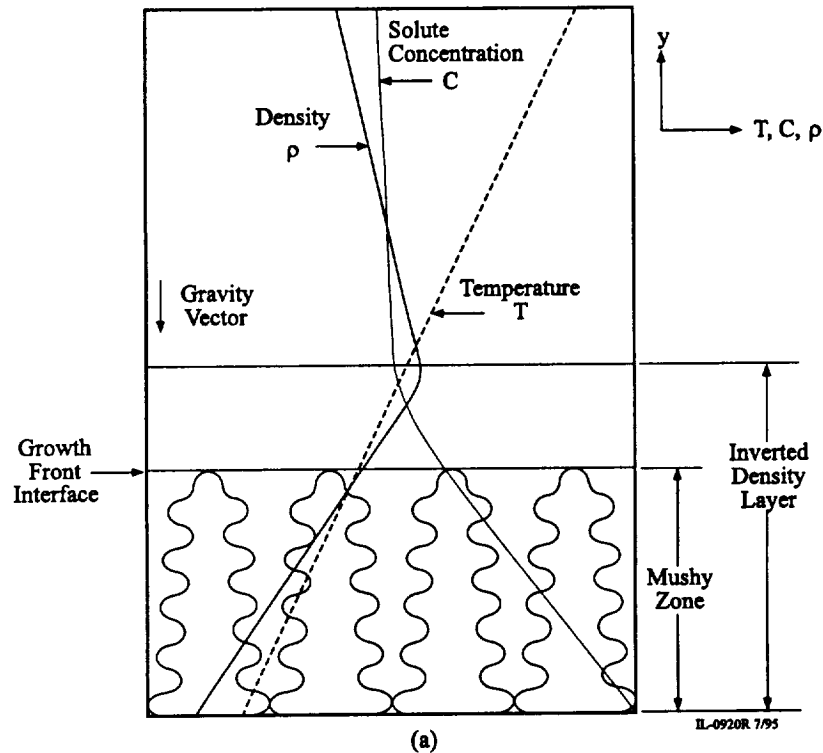


Figure 1. (a) Density Profile in the Dendritic $\text{NH}_4\text{Cl-H}_2\text{O}$ System and (b) Cuvette and Solidification Assembly Schematic.

The properties of room temperature liquid NH_4Cl -72 wt% H_2O are given in Table 1. The index of refraction variation with temperature and concentration for concentrations around 72 wt% H_2O and temperatures near room temperature has been fitted to yield.¹³

$$n = 1.63 \pm 0.11 \times 10^{-3}(C - 27.07 \text{ wt}\%) + 1.337 - 1.73 \pm 0.25 \times 10^{-4}(T - 22^\circ\text{C})$$

(Note: All nomenclature is defined in the Appendix: Nomenclature.) If the temperature within the NH_4Cl - H_2O solution can be independently measured, the index of refraction field in the fluid can be used to determine the solutal field.

TABLE 1

Table of Properties of 28 wt% NH_4Cl - H_2O

• Heat of Solution (25°C)	66.04 cal/gm
• Specific Heat	0.789 cal/gm°C
• Liquidus Temperature	23.7°C
• Partition Coefficient	0.0039
• Diffusion Coefficient (28% NH_4Cl)	$2.302 \times 10^{-3} \text{ cm}^2/\text{sec}$
• Surface Tension	76.3 dynes/cm
• Surface Energy	40 (+/-10) erg/cm ²
• pH	5.0
• Density (25°C)	1.0767 gm/cm ³
• Viscosity (25°C)	1.058 poise
• Index of Refraction (25°C, 632.8 nm)	1.3836
• Eutectic T°	-15.4°C
• Eutectic Composition	19.7 wt%
• Liquid Fraction at Eutectic T°	89%
• Thermal Conductivity	$1.204 \times 10^{-3} \text{ cal/cm} \cdot \text{sec}^\circ\text{C}$
• Thermal Diffusivity	$1.5 \times 10^{-3} \text{ cm}^2/\text{sec}$
• Grashof Number (Gr)	10
• Solutal Grashof Number (Gr_s)	6.2
• Prandtl Number (Pr)	7
• Lewis Number (Le)	65
• Schmidt Number (Sc)	400
• Thermal Expansivity ($^\circ\text{C}^{-1}$)	2.95×10^{-4}
• Solutal Expansivity (wt% ⁻¹)	-2.81×10^{-3}

university/prop/subject95tab1

Ground-Based Solidification System

The cuvette and necessary thermal control assemblies were designed for use with a variety of optical systems to allow for maximum flexibility. A quartz cuvette containing NH_4Cl - H_2O solution was placed within the optical object plane. Thermoelectric devices at the top and bottom surfaces of the cuvette were used to produce the temperature gradient and the heating and cooling profiles. Temperatures were monitored with chromel-alumel thermocouples both inside (sometimes) and on the outer side wall surfaces (always) of the cuvette. A PC based system controlled the run profile which consisted of first establishing a linear thermal gradient (G) and then simultaneously lowering both top and bottom temperatures at a desired cooling rate (CR). Figure 1 includes a schematic of the cuvette

solidification assembly. A complete description of the entire assembly is published in References 14 and 15.

Ground-Based Experimental Optical Methods

Four types of optical diagnostic procedures have been used to investigate and quantify the solidification phenomena: 1) Particle tracking for depicting flow patterns, 2) schlieren and 3) central dark ground methods of phase contrast to examine diffusion layer growth and plume behavior, and 4) Mach-Zehnder interferometry for quantitative measurements of temperature and concentration distributions. As solidification progressed, the optical data were stored on video tape. Temperature and time data were stored on computer disk. This permitted post-experiment processing of all data and the application of sophisticated computer image processing techniques to maximize the optical data accuracy.

Particle Tracking

In particle tracking, the fluid is doped with small quasi-neutral density particles which scatter light but introduce negligible changes in the fluid properties. A sheet beam of light (0.6 watt Argon-Ion Laser) is directed through the fluid to illuminate the particles in a chosen plane. Movement of the particles is then observed, providing data regarding flow geometry and fluid velocities. By use of time exposure photography, small velocity flow fields can be visualized and measured. This technique was used by the investigators to characterize the behavior of the convective breakdown which occurred within the diffusion layer ahead of the solidifying interface.¹⁶ This was the first observation of this behavior and was found to constantly precede the development of plumes and chimneys which are generally accepted as responsible for channelling.

A second analysis system is the Particle Displacement Tracking (PDT) apparatus. Again, the system centers around the solidification assembly. The ammonium chloride solution in the cuvette is seeded with 50 μm polystyrene particles which are illuminated by white fiber optic lights during solidification. Two orthogonal planes within the cuvette are viewed by CCD cameras equipped with 0.5 mm focal depth microscope lenses, and the images are recorded on videotape. The videotape is processed using Data Translation image processing hardware and software along with specially developed software to obtain velocity vector plots of the particles in the fluid.

Confocal Optical Signal Processing

Both the schlieren and the central dark ground methods employ a confocal optical signal processing system. This system consists of two identical lenses separated by a distance of two focal lengths, $2f$. An object in the front focal plane of the first lens thus forms a real image at unit magnification in the back focal plane of the second lens. According to scalar diffraction theory, the field in the back focal plane of the first lens (located midway between the two lenses) is the two-dimensional Fourier transform of the field in the front focal plane with the spatial frequency variables given by¹⁷

$$f_x = \frac{x}{\lambda f}, \quad f_y = \frac{y}{\lambda f}$$

By placing appropriate filter screens in this Fourier plane, the spatial frequency content of the light field can be altered. The resulting image is thus a filtered version of the incident object field. The effect of the filter screen on the resulting image can then be described by linear systems for signal processing.

For the familiar schlieren method of phase contrast, a knife edge is placed in the Fourier plane to block half of the diffracted light. The resulting image intensity distribution can be written¹⁷

$$I_i(x, y) = \frac{1}{4} \left[V_0(x, y) + \frac{i}{\pi} \int_{-\infty}^{\infty} \frac{V_0(x, \eta) d\eta}{y - \eta} \right]^2$$

for a horizontally oriented knife edge. Although the intensity distribution of the schlieren image is difficult to interpret quantitatively, the method has the advantages of simplicity and ruggedness and performs extremely well in the visualization mode.

The central dark ground method of phase contrast consists of placing a small opaque obstruction in the Fourier plane of the optical signal processing system.^{17,18} This effectively removes low frequency components from the diffracted field, thus resulting in an output image intensity distribution which, with appropriate approximations and substitutions, can be given by

$$I_i(x, y) = (A_0^2 + B_0^2) \left(1 - \frac{2a_0 B_0}{A_0^2 + B_0^2} \cos[\phi(x, y) - \phi_0] \right)$$

The image consists of light and dark fringes. The intensity reaches a minimum whenever the argument of the cosine is an even integer multiple of π . This technique can be used to make quantitative measurements of temperature and concentration within the solidifying solution¹⁹ but low fringe visibility can sometimes present a problem. Thus the principal utility of this method is measuring the height of the water-enriched diffusion layer since the region of density inversion for an image processed in this manner appears as a distinctive dark band, i.e., null, the height of which (above the interface) is easily measured. This method also allows growth rate determination and the visual observation of the diffusion layer and the occurrence of the pattern of the flow at convective breakdown.¹⁹

Interferometry can be used for making the quantitative measurements of the temperature and concentration distribution within the solidifying system. In a Mach Zehnder interferometer, part of the incident radiation in the collimated beam is removed before it passes through the test section and later recombined with the signal beam. The amplitude of the reference beam can be controlled to equal that of the beam passing through the solution. The resulting image intensity can be written

$$I_i(x, y) = 2A_0(1 + \cos[\phi(x, y) - \phi_0])$$

The intensity reaches a minimum for every 2π phase shift between the reference and signal beam, similar to the central dark ground method. However, the fringe visibility is much higher allowing for accurate spatial measurement of the location of the fringe centers. This data is then used for calculating the temperature and concentration distributions within

the fluid. Visual observation of the interface and breakdown behavior is also possible with this technique.

Figure 2 shows schematics of three of the optical systems used in the various CAST ground based experiments. As seen in Figure 2(a), the central dark ground processor and the particle tracking technique were applied to one solidification system to obtain simultaneous flow and optical phase measurements. Table 2 lists the four optical techniques discussed along with the qualitative and quantitative information that can be obtained from each. As can be seen, each technique contributes uniquely to the overall experimental program.

TABLE 2

Optical Technique	Qualitative Information	Quantitative Information
Particle Tracking	Flow Geometry	Cell Wavelength Flow Velocities
Schlieren	Plume Occurrence Interface Shape	Plume Movement Growth Rates
Central Dark Ground	Breakdown Occurrence Cell Behavior	Diffusion Layer Height Null size Growth Rates
Interferometry	Breakdown Occurrence Cell Behavior Interface Shape	Temperature Distribution Concentration Distribution

nmayreport/cle95tab2

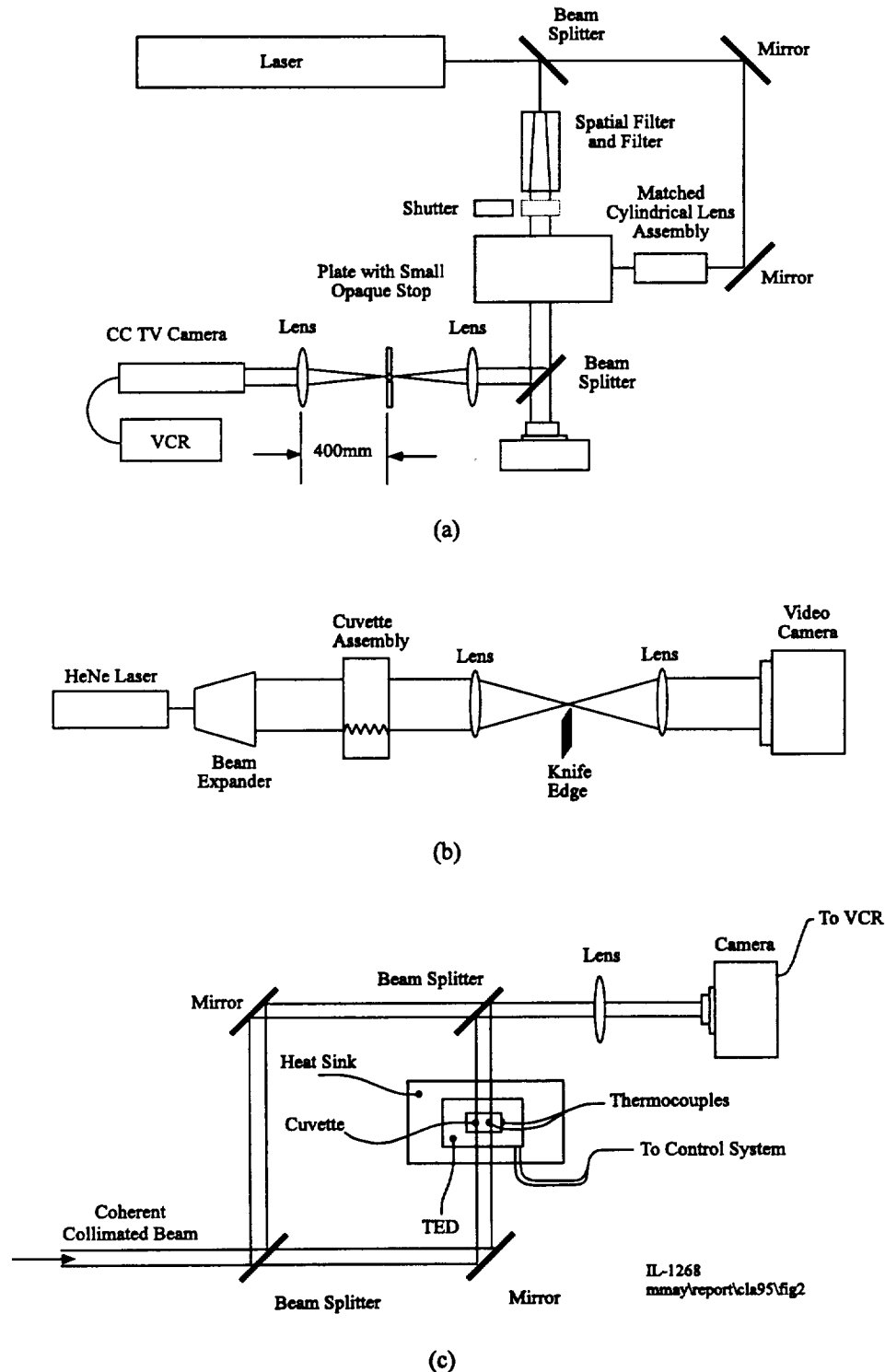


Figure 2. Schematic of CAST Ground-Based Optical Assemblies (a) Central Dark Ground Confocal Optical Processing and Particle Tracking (b) Schlieren Confocal Optical Processing and (c) Mach-Zehnder.

Holographic Reconstruction

Since a holographic system was used on the spacelab flight to record the CAST optical data, a holographic reconstruction system was assembled in the UTSI laboratory.²⁰ A beam duplicating the original reference beam is passed through the hologram at the same angle as when it was created, thus recreating the original object beam. The image can then either be recorded by camera as shown on the schematic in Figure 3, or can be optically processed by techniques such as discussed above. The UTSI holographic reconstruction system was designed to include a Mach Zehnder interferometer. The shaded portion of Figure 3 indicates the optical components added to enable interferometry. This system was used to obtain quantitative information from the flight holograms taken aboard IML-1.

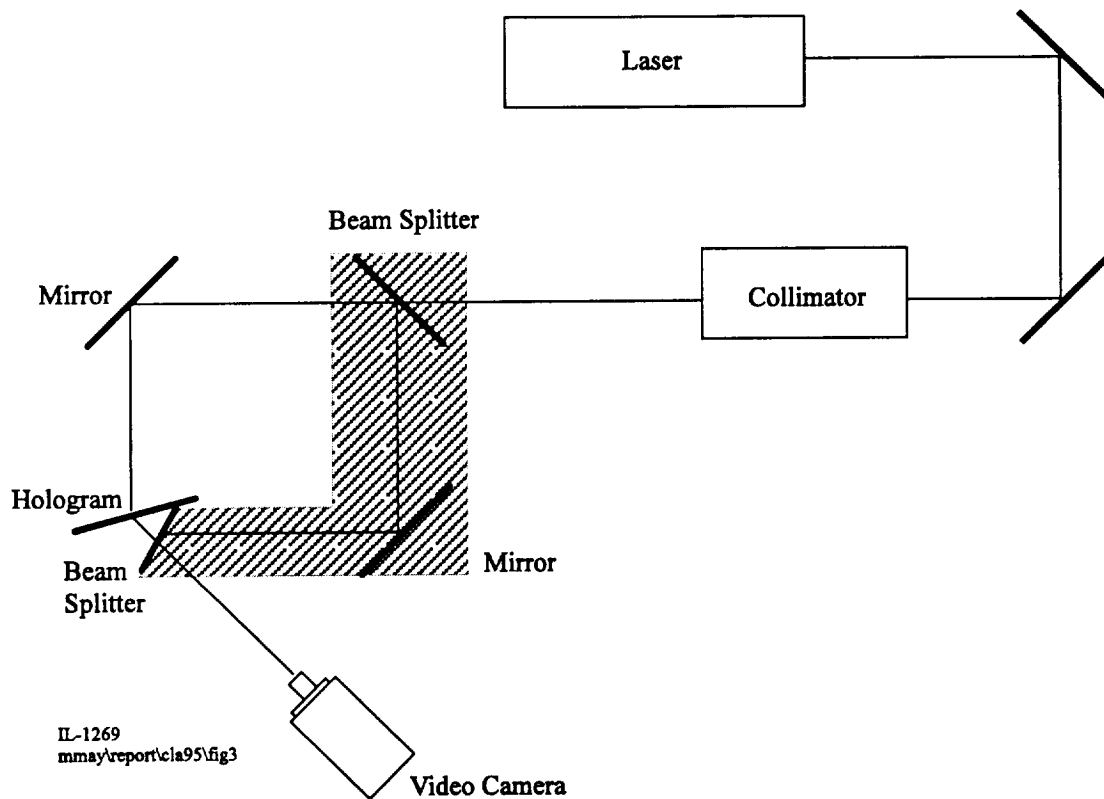


Figure 3. Schematic of UTSI Holographic Reconstruction System with Mach Zehnder Interferometer.

Image Analysis

As mentioned earlier, images from the ground-based experiments were recorded on videotape. The quantitative information listed in Table 2 can then be obtained using image analysis techniques. The temperature and concentration distribution are determined from the fringe patterns using either an intensity technique or a spatial phase technique.

The intensity technique tracks the fringe extrema. Each fringe represents a phase change of 2π and information between the fringes is lost. Figure 4²¹ shows a sequence of interferometer photographs during the evolution of the diffusion layer in front of a growing $\text{NH}_4\text{Cl-H}_2\text{O}$ interface. The middle of each fringe can be located either by a cursor operator or automatically by maximum pixel intensity. The fringes above the diffusion layer are used to calculate the temperature gradient since, barring vigorous convection, the liquid is of uniform concentration in that region. This temperature gradient is then used with the measured index of refraction field in the diffusion layer to calculate the concentration differences relative to the region above the interface. This technique allows the information to be obtained only at discrete points associated with the fringe locations. An exponential curve fit is applied to these data, providing concentration versus height curves at selected times. Each profile is fit to the form

$$C(y) = (C_t - C_0)e^{-\psi y} + C_0$$

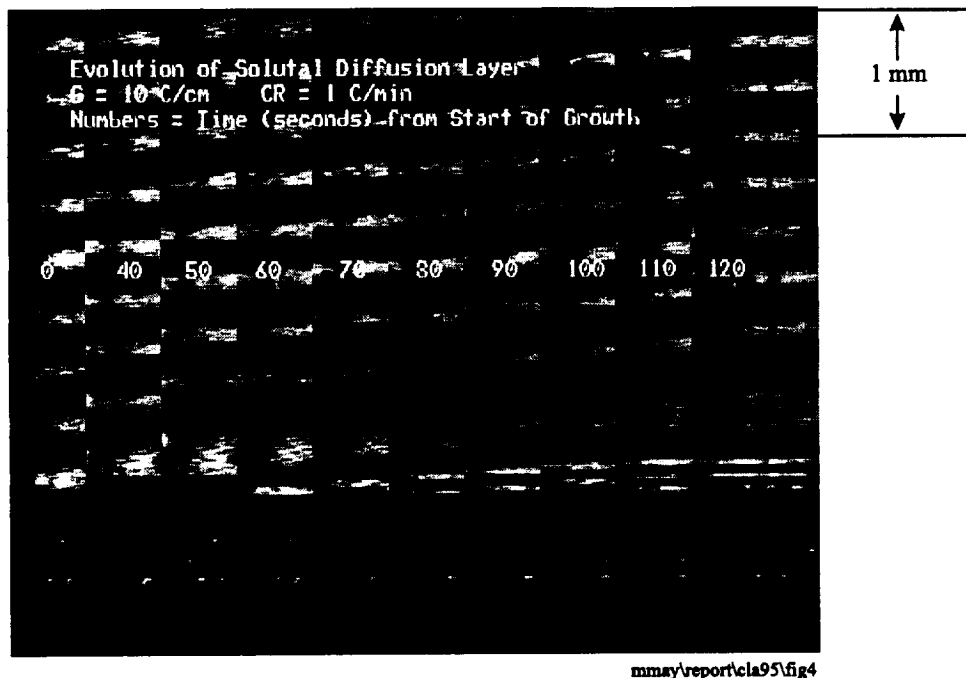


Figure 4. Evolution of Solutal Diffusion Layer for $CR = 0.017 \text{ C/sec}$.

This provides the tip concentration, C_t and an exponential diffusion length scale analogous to R/D for steady state growth. Figure 5 gives the diffusion layer concentrations obtained by this method for specific times during one ground-based experiment. These measurements represented the first in-situ, real time (recorded), non-interfering measurements of solutal layer growth in a dendritic system.

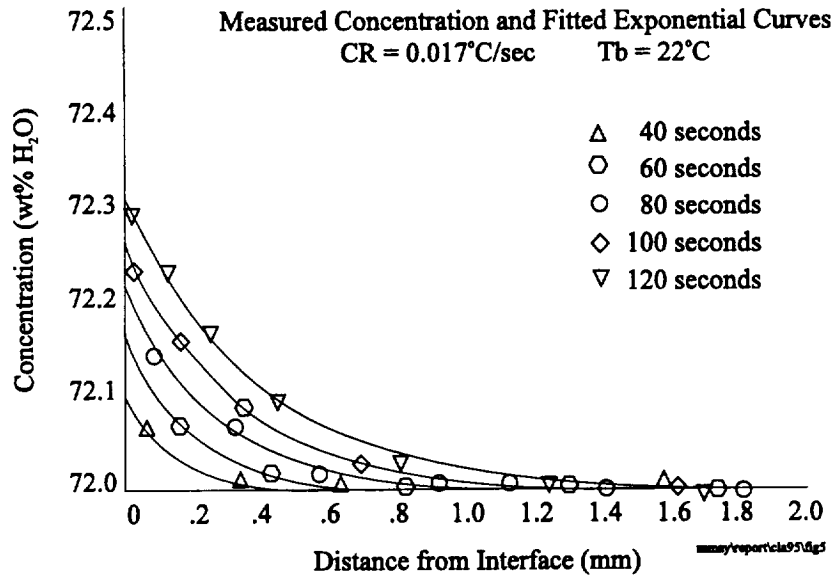
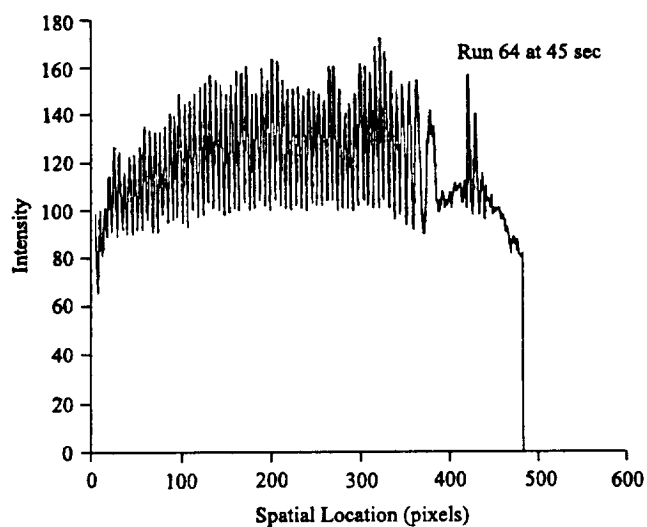
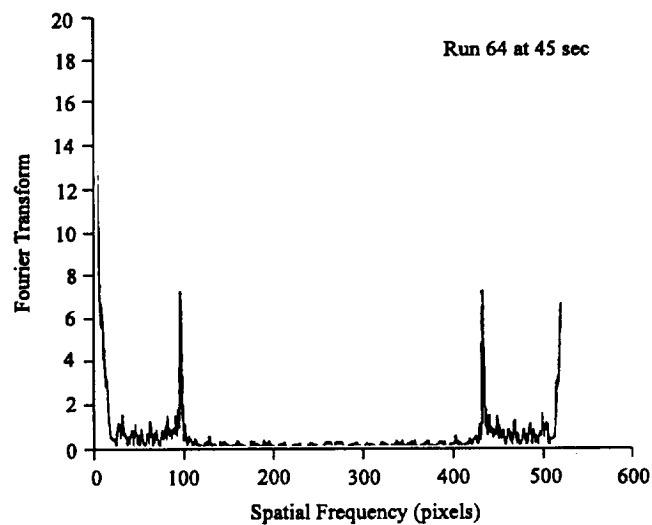


Figure 5. Measured Concentration for $CR = 0.017$ C/sec and $T_b = 22$ C.

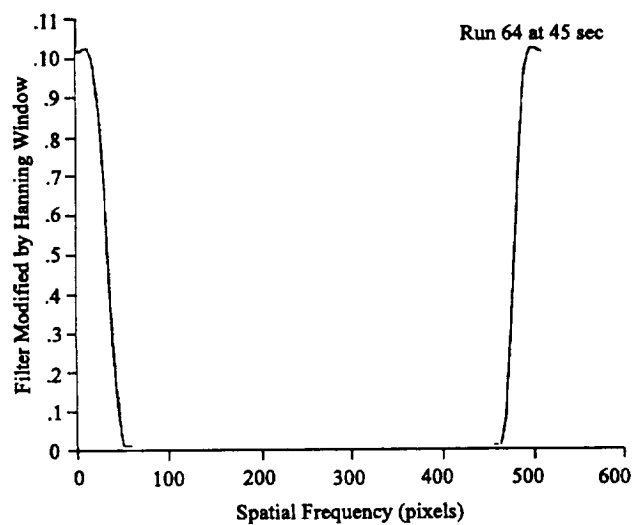
The spatial phase technique introduces a known phase shift which produces a carrier image over the extent of the interferogram. This is usually accomplished by a tilt in the reference beam. The Fourier-transform method developed by Takeda²² was selected for application to the CAST experiments. Advantages of this spatial technique are its amenability to automated image analysis and its use of all of the phase information rather than just the phase extrema. This means that very low index of refraction variations (i.e., those producing less than 2π phase shifts) can be measured. Details of this and other techniques investigated are given in Reference 20. In general, the procedure is as follows: 1) One of the digitized data columns from the image above the interface is selected, 2) a plot of the intensity of the image is produced, 3) the Fourier transform is produced and plotted, 4) cutoff frequencies for a lowpass filter are selected, 5) the lowpass filter is applied, 6) the phase is computed, 7) the effects of the carrier image and the temperature gradient are subtracted, 8) the index of refraction is calculated, 9) the concentration is determined. Steps one through six are applied individually to the carrier image and the experimental image obtained during directional solidification. The final steps manipulate the corrected experimental information. Figure 6²⁰ depicts the results as the procedure is applied to one video frame of interferometer data.



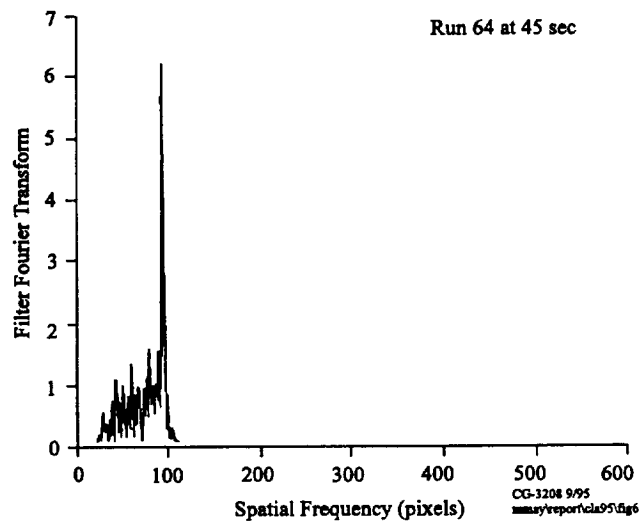
(a)



(b)



(c)



(d)

Figure 6. Images 28 from the Spatial Phase Fourier Transform Technique (a) Experimental Image Intensity, (b) Fourier Transform, (c) Filter Modified by Hanning Window, (d) Filtered Fourier Transform.

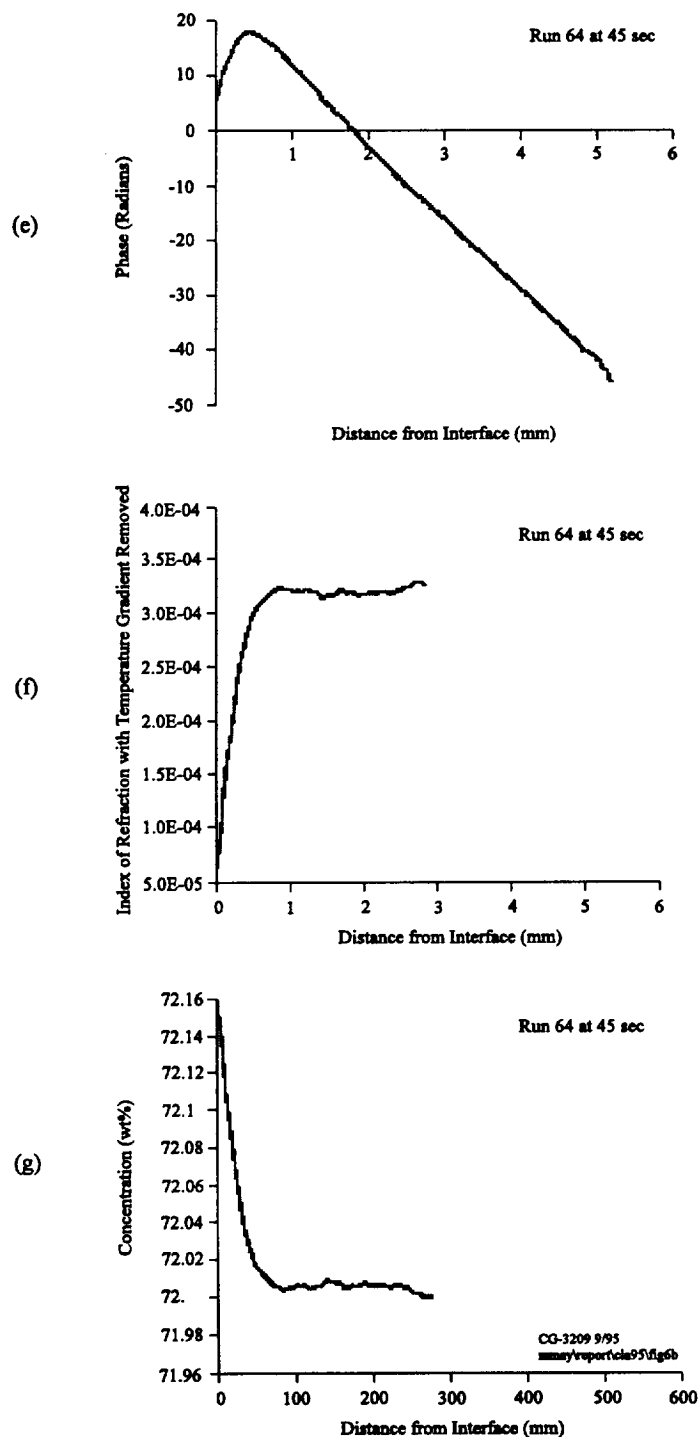


Figure 6. (Cont'd). Images 28 from the Spatial Phase Fourier Transform Technique (e) Phase, (f) Index of Refraction, and (g) Concentration.

The particle displacement tracking (PDT) images were recorded on videotape at seven different locations (planes) in the cuvette. The spacing between locations was selected to be .5mm. This process is performed for both cameras, giving a set of images for each viewing direction. A single VCR was used for both cameras with a video mixer routing the desired signal. The third camera was used to measure interface height as a function of time.

The recorded video images were analyzed using a PDT approach.^{23,24} In this method, video frames are digitized and analyzed in an automated fashion to construct two-dimensional velocity fields. The image analysis procedure consisted of transferring the images from videotape to optical disc, digitizing selected frames, and analyzing these frames using the PDT procedure. The system used a Panasonic laser optical disc recorder and a Data Translation digital image processor with host PC computer. After the recorded video was transferred to optical disc, the images could be displayed frame by frame on a digital image processing system without the synchronization and noise problems of single frame manipulating characteristic of VCRs. Approximately 30 frames (1 second of experiment time) for each plane, at each time of interest were recorded on the optical disc. Selected frames were then digitized in an 8-bit 512 × 512 format for analysis using the image processing system.

The PDT procedure itself consists of two primary steps: 1) determining particle centroid location, 2) tracking the particle displacement. Although details of the particle location and vector calculation routines can be found in the literature and in the software documentation, several modifications were necessary to provide the flexibility and robustness necessary for this application and thus, a general overview is provided for completeness.

The PDT technique consists of analysis of five sequential, digitized video images which have been processed (equalized) to enhance the particle contrast. After equalization, the image intensity of the pixels representing the particles are all above a threshold level. For each image, a gradient-based edge detection algorithm is used to search for particles in a specified window within an image. Once an edge is located, this represents the edge of a potential particle. The perimeter of the particle is traced in a clockwise boundary-following search to determine the exact size and centroid location of the particle. If the perimeter of the particle is within specified limits, the particle information is stored, otherwise it is discarded as a false particle. The edge-detection and boundary-following search algorithms are additions to the base PDT algorithm which allows for the robust identification of non-circular particles.

Once a particle is found, the location of the particle centroid is calculated and stored, the intensity of the searched area is set to zero to prevent future use, and the search is continued for remaining particles. This is repeated for the five images and all of the particle centroid locations are stored on a single skeletonized image. The pixel intensities at the particle centroids are scaled based on the frame from which the particles originated (intensity = $2n$ where n = frame #), and the resulting image is processed to determine the velocity field.

A search is made starting with all frame one particles to determine the probable particle locations in the other frames. All frame two particles within a given radius of the

frame one particles are potential candidates for lying on the correct vector. The search continues from frame two particles to frame three particles and so on until a consistent vector is found (if one exists) for particles from all five frames. Another modification to the PDT algorithm is implemented in the vector determination procedure. This consists of an allowance for variations in the vector direction from frame to frame. This allowance is typically 1-2 pixels, and allows for slight turning of the flow. Thus for a successful search, a unique set of approximately collinear particles each separated by a distance less than the maximum search radius must be found. Typically, at least 40 vectors were identified from more than 300 particles for the images in this study. Figure 7 depicts a typical velocity field image.

The original search and vector determination algorithms were developed at Lewis Research Center (LRC) and are available through COSMOS.²⁴ The original routines were written for the specific image processing hardware used at LRC, but are easily adapted for use with other image formats. In addition to modifying the format of the input image files and extending the centroid location and velocity determination algorithms, the graphical user interface coded in the COSMOS software was removed. Although the programs were developed using the MicroWay DOS extended FORTRAN compiler, they ran with little modification using the Microsoft FORTRAN Power Station compiler and DOS extender.

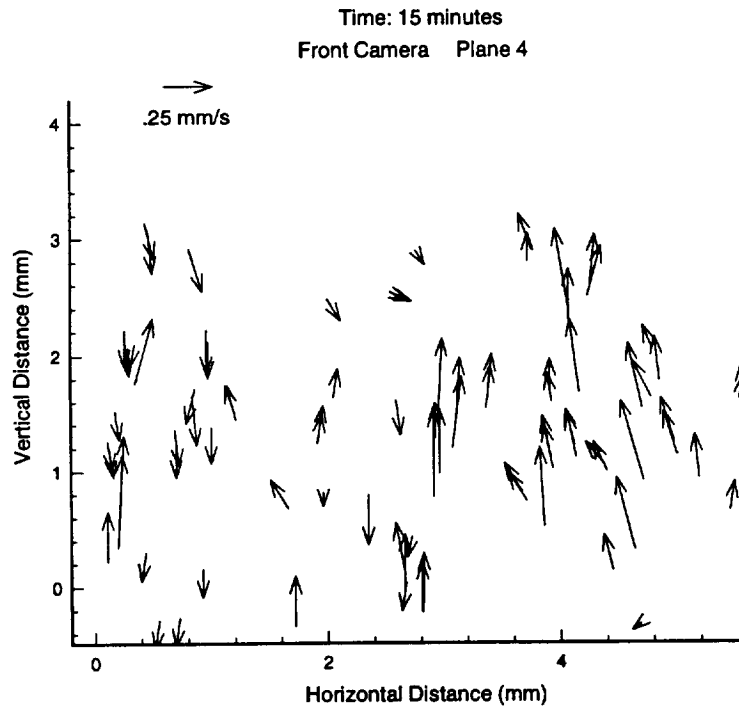


Figure 7. Velocity Field at 15 minutes for no-plume case (front camera, middle plane).

CAST Fluids Thermal Model (FTM)

In support of the CAST solidification study, a numerical model²⁵ was developed to help analyze the ground-based data and to provide predictions for the upcoming IML-1 Spacelab experiments. The code predicts the development of the solutal and thermal fields and the local percent of solid and liquid for ammonium chloride and water during solidification. While primarily intended to model diffusion dominated directional solidification in microgravity, the code calculates both contraction and buoyancy driven flows and is also capable of analyzing the 1 g_e ground-based data.

Initial comparisons between the code predictions and ground-based results served as model verification. The discrepancies between initial numerical predictions and the ground-based experimental results conclusively determined that undercooling effects must be appropriately included in modeling directional solidification for this system. This is in contrast to the assumption of equilibrium common in most solidification models. In order to correct this deficiency, a set of criteria for solidification was incorporated into the code. A parametric study²⁶ has recently been completed indicating the effectiveness of those criteria.

The numerical model is capable of simulating the experiment up until the onset of vigorous (chaotic) convection. The model's accuracy can be measured by how well it predicts the observed growth of the mushy zone, the extent and stability of the density inversion, and the solutal and thermal distributions within the inversion layer.

Numerical Model

The numerical technique used in the code is an established conservative control volume scheme²⁷ extended to include the effects of two-phase flow.^{28,29} The program solves for the conservation of mass, species, momentum and energy based on a set of continuum conservation equations derived for multiphase flow.²⁵ The modified equations, as used in the model, are listed below. The energy equation used is:

$$\frac{\partial}{\partial t} \left[\left(g_l \rho_l \frac{\partial h_l}{\partial T} + g_s \rho_s \frac{\partial h_s}{\partial T} \right) T \right] + \nabla \cdot \left[g_l \rho_l \mathbf{V}_l \frac{\partial h_l}{\partial T} T \right] = \nabla \cdot [(g_s k_s + g_l k_l) \nabla T] + S$$

where

$$S = \frac{\partial}{\partial t} \left[g_l \rho_l \frac{\partial h_l}{\partial T} T_0 + g_s \rho_s \left(\frac{\partial h_s}{\partial T} T_0 - \frac{\partial h_s}{\partial C_s} (C_s - C_0) - h_{s0} \right) \right] \\ + \nabla \cdot \left[g_l \rho_l \mathbf{V}_l \left(\frac{\partial h_l}{\partial T} T_0 \right) \right]$$

Implicit in the above energy equation are the assumptions that the individual enthalpies of the liquid and solid can be expressed in terms of temperature and concentration using a two-dimensional Taylor series expansion, and that the temperature of the liquid and solid at a point are the same. The corresponding solutal equation used in the numerical model is,

$$\frac{\partial}{\partial t} (g_l \rho_l C_l) + \nabla \cdot [g_l \rho_l \mathbf{V}_l C_l] = \nabla \cdot [g_l \rho_l D_l \nabla C_l] \\ + \nabla \cdot [g_s \rho_s D_s \nabla C_s] - \frac{\partial}{\partial t} (g_s \rho_s C_s)$$

where it is assumed that diffusion in the solid can be neglected for ammonium chloride and water and that once formed the solid remains fixed ($\mathbf{V}_s = 0$). The later assumption of no flow of the solid can also be used to simplify the conservation of momentum equation giving (in the horizontal direction):

$$\frac{\partial}{\partial t}(\rho_l g_l u_l) + \nabla \cdot (\rho_l g_l \mathbf{V}_l u_l) = \nabla \cdot (\mu_l \nabla(g_l u_l)) - \frac{\partial \rho}{\partial x} + \rho B_x - \frac{\mu_l}{K_x} g_l u_l$$

In order to compute the solution for a given case, the experimental domain is divided into numerical control volumes and the conservation equations are discretized so they can be applied to each cell in turn. The code iterates over the domain for a given time until the conservation equations and boundary conditions are mutually satisfied. During the iteration process, the extent of solidification within a control volume is governed by a combination of the equilibrium phase diagram and three nucleation (undercooling) criteria. With these nucleation criteria in effect, a numerical cell whose temperature and solutal concentration place it below the liquidus does not necessarily begin to solidify. Instead, one of the following three conditions must be met prior to the formation of solid in that cell: 1) if solid existed in the cell at the last numerical time step, then additional solidification is allowed based on the equilibrium phase diagram, 2) if the liquid in the cell becomes undercooled by a prescribed amount, then spontaneous solidification is permitted, regardless of whether solid previously existed in that cell, 3) if any of the neighboring cells contain more than a nominal value of solid volume fraction, then solidification in the central cell is allowed. This criterion is based on the geometrical argument that above the threshold value the neighboring dendrites would provide a growth site for solidification. This criteria can be extended to include the presence of a growth surface as the wall.

Code Validation

Several publications^{25,30} dealing with validating the code have already been published and a final one²⁶ which details the recently conducted sensitivity studies is in preparation. Therefore, only a few of the comparison results will be presented here. The model was used to predict solidification for a ground-based experiment with a cooling rate of 2°C, initial top and bottom temperatures of 58.5°C and 21°C, respectively, and a solutal concentration of 72 wt% water. Figure 8 presents a comparison between the predicted and measured solidification front location for both equilibrium and non-equilibrium predictions. The non-equilibrium values fall very near to the experimental points. The equilibrium calculation is seen to be badly in error.

The code also calculates the complete solutal and thermal field distribution throughout the solution. These fields are responsible for the diffusion driven convective breakdown which occur ahead of the dendritic layer. The predicted solutal distribution ahead of the mushy zone (MZ) correlates well with the experimental data as shown in Figure 9. In addition, the predicted time of convective breakdown (as indicated by the calculated total kinetic energy in the numerical domain) is realistic when undercooling effects are included as shown in Figure 10. This is true despite the fact that convective breakdown is a complicated function of both growth and undercooling conditions. A large number

of computations using the model to predict thermal only (Rayleigh) breakdown and a multitude of solidification cases have all shown the code predictions to be reliable for the range of variables considered in the CAST ground-based and IML-1 experiments. The calculated critical Rayleigh number as determined from Figure 10 is also consistent with those determined in the laboratory.³¹

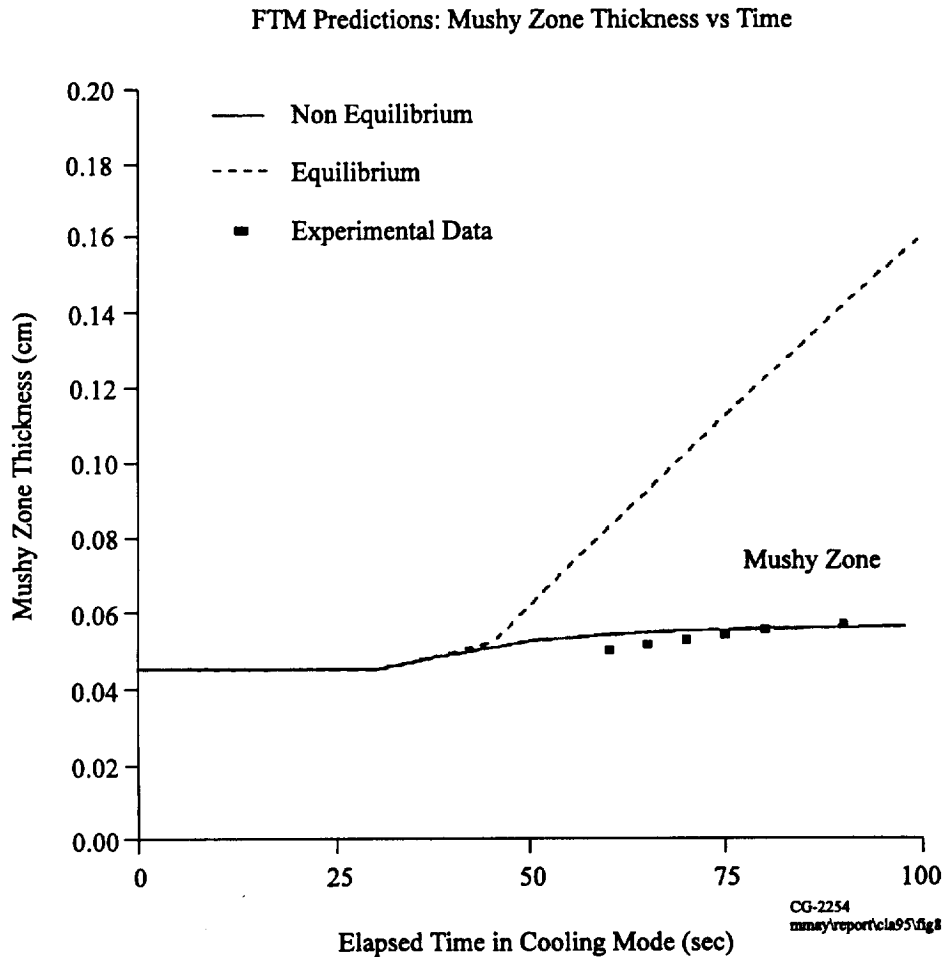


Figure 8. Variation of Mushy Zone Height with Time.

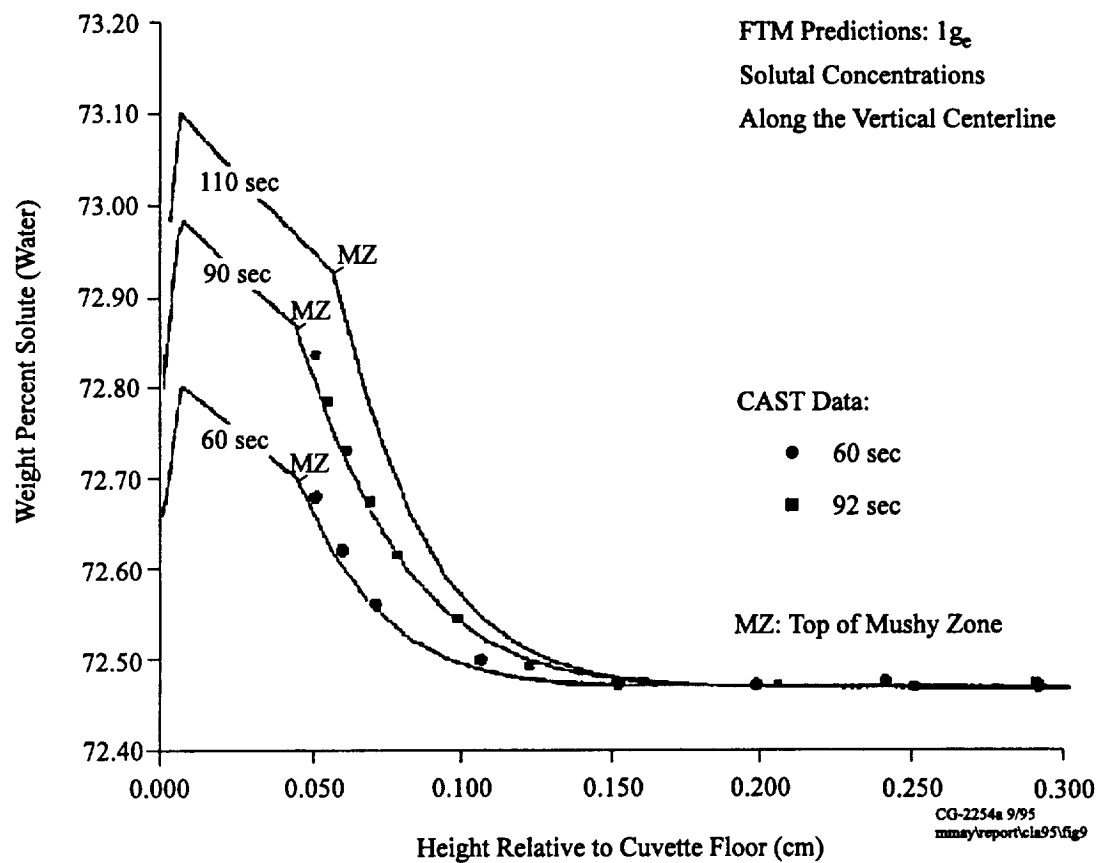


Figure 9. Solutal Concentration Profile Changes with Time.

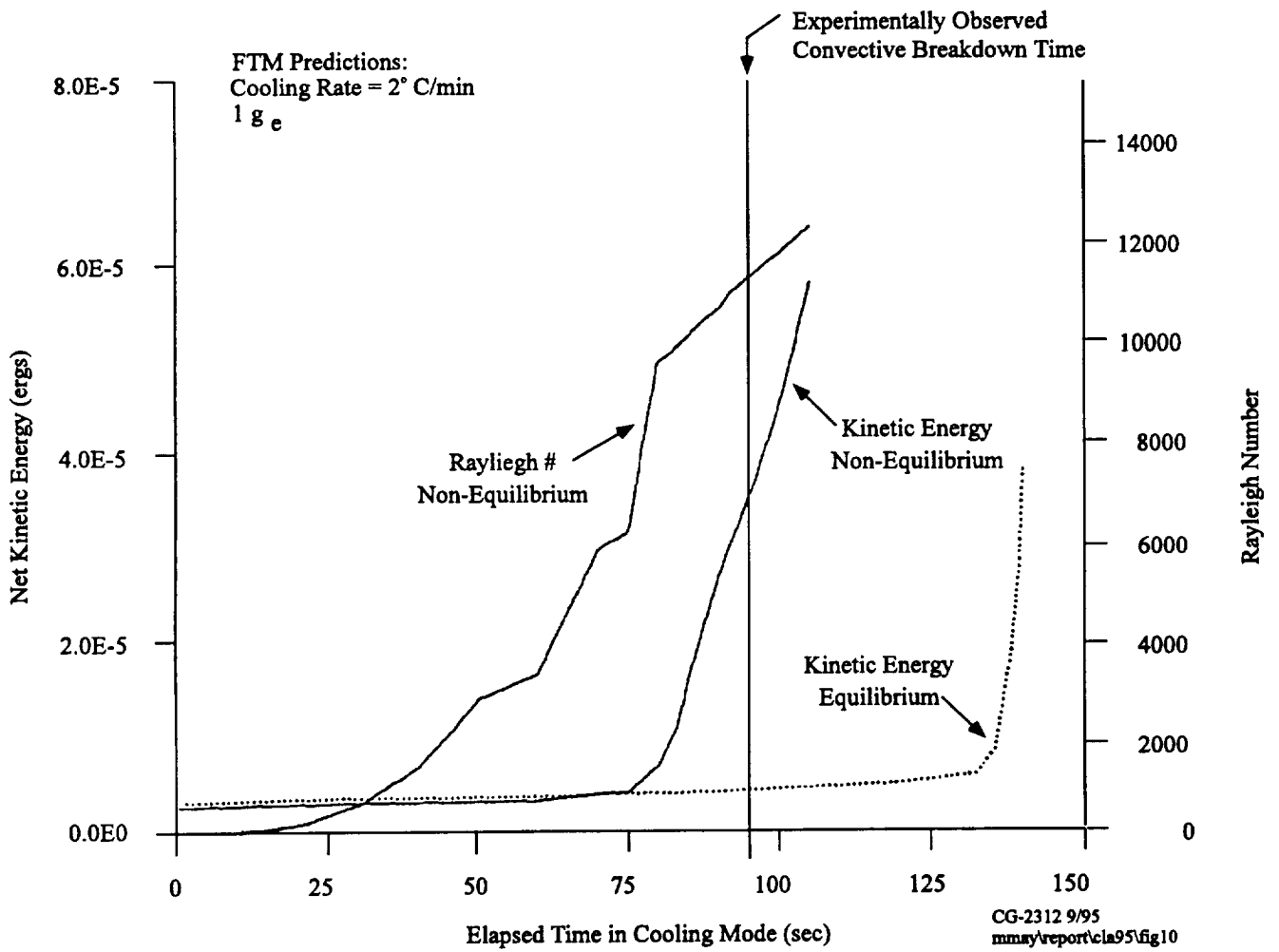


Figure 10. Predicted Net Kinetic Energy.

Sensitivity Studies

The sensitivity of the nucleation (undercooling) model to the grid size, the time step size, and the choice of threshold value for the neighboring cell was tested by using the parameters in Table 3. This was deemed necessary since the non-equilibrium assumptions so strongly influenced the predicted behavior.

TABLE 3

PARAMETER	CASE 1	CASE 2	CASE 3
Grid	10 x 110	30 x 110	10 x 66
Time Step	1 sec	1 sec	1 sec
Neighbor g_i Threshold	.99	.99	.99
Max Undercooling	15°C	15°C	15°C
Gravity Level	$1 \times 10^{-3} g_e$	$1 \times 10^{-3} g_e$	$1 \times 10^{-3} g_e$
Cooling Rate	2°C/min	2°C/min	2°C/min
Initial Top Temp	58.5°C	58.5°C	58.5°C
Initial Bottom Temp	21°C	21°C	21°C
Heat Loss Coefficient	$0 \frac{\text{ergs}}{^\circ\text{C} \cdot \text{cm}^2}$	$0 \frac{\text{ergs}}{^\circ\text{C} \cdot \text{cm}^2}$	$0 \frac{\text{ergs}}{^\circ\text{C} \cdot \text{cm}^2}$
Bulk Loss Coefficient	72 wt% H ₂ O	72 wt% H ₂ O	72 wt% H ₂ O
Permeability const. K_0	$5.56 \times 10^{-7} \text{ cm}^2$	$5.56 \times 10^{-7} \text{ cm}^2$	$5.56 \times 10^{-7} \text{ cm}^2$

PARAMETER	CASE 4	CASE 5	CASE 6
Grid	10 x 66	10 x 66	10 x 66
Time Step	.2 sec	10 sec	1 sec
Neighbor g_i Threshold	.99	.99	.99
Max Undercooling	15°C	15°C	15°C
Gravity Level	$1 \times 10^{-3} g_e$	$1 \times 10^{-3} g_e$	$1 \times 10^{-3} g_e$
Cooling Rate	2°C/min	2°C/min	2°C/min
Initial Top Temp	58.5°C	58.5°C	58.5°C
Initial Bottom Temp	21°C	21°C	21°C
Heat Loss Coefficient	$0 \frac{\text{ergs}}{^\circ\text{C} \cdot \text{cm}^2}$	$0 \frac{\text{ergs}}{^\circ\text{C} \cdot \text{cm}^2}$	$0 \frac{\text{ergs}}{^\circ\text{C} \cdot \text{cm}^2}$
Bulk Loss Coefficient	72 wt% H ₂ O	72 wt% H ₂ O	72 wt% H ₂ O
Permeability const. K_0	$5.56 \times 10^{-7} \text{ cm}^2$	$5.56 \times 10^{-7} \text{ cm}^2$	$5.56 \times 10^{-7} \text{ cm}^2$

All of the runs were started from the same set of numerical initial steady state.

mmayrep01a95tab3

In order to test the sensitivity of the nucleation criteria to grid size, identical simulations were computed using a fine, medium and coarse grid (Case 1-3). The plots of the resulting mushy zone height in Figure 11 show that the growth rate, as influenced by the nucleation criteria, is relatively insensitive to the grid structure. This is, in particular, demonstrated by the coarse grid (Case 3) which has twice the vertical grid spacing of the other two, and yet gives very similar growth rates. (The time required to compute the coarse grid results was 1/40 of that required for the fine grid.) The major difference between the coarse grid results and the other two is the initial height of the mushy zone. This difference occurs because the coarse grid does not have sufficient resolution to predict the small initial layer that exists for the given boundary conditions. As such, it is not a manifestation of the nucleation criteria.

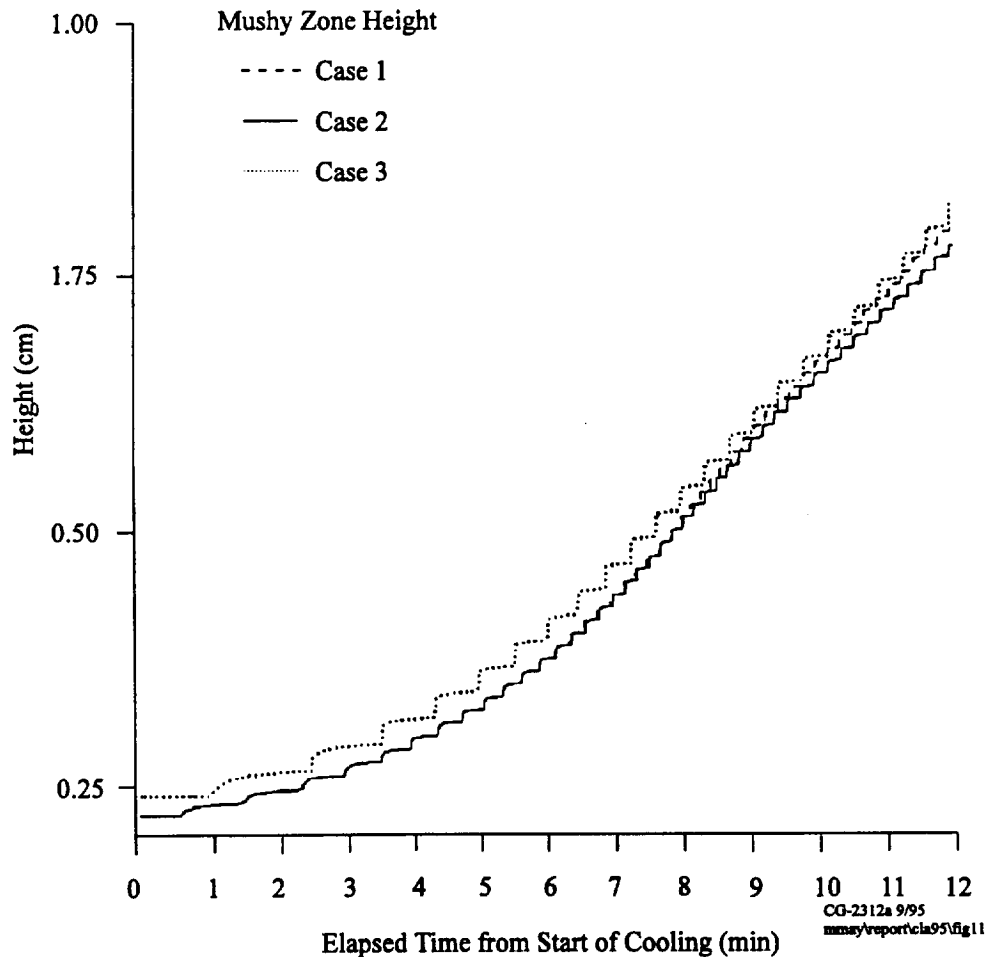


Figure 11. Grid Dependence (Case 1-3): Mushy Zone Height vs. Time.

The sensitivity of the undercooling model to the time step was tested using the coarse grid and three different time steps (Cases 3-5). For a relatively large time step, the nucleation criteria will be adversely affected since the comparisons in the undercooling checks use previous time step values to ensure numerical stability. As a rule of thumb, if the solidification front is advancing one cell at each time step, then nucleation criteria may inhibit growth, and a smaller time step is needed. For the case shown in Figure 12 the growth rate is well below this limit with the result that the time steps of .2 seconds and 1 second give identical results. Even the relatively large time step of 10 seconds gives similar results. (The later time step reduces the computation time on a desktop 386 to real time for the given case.)

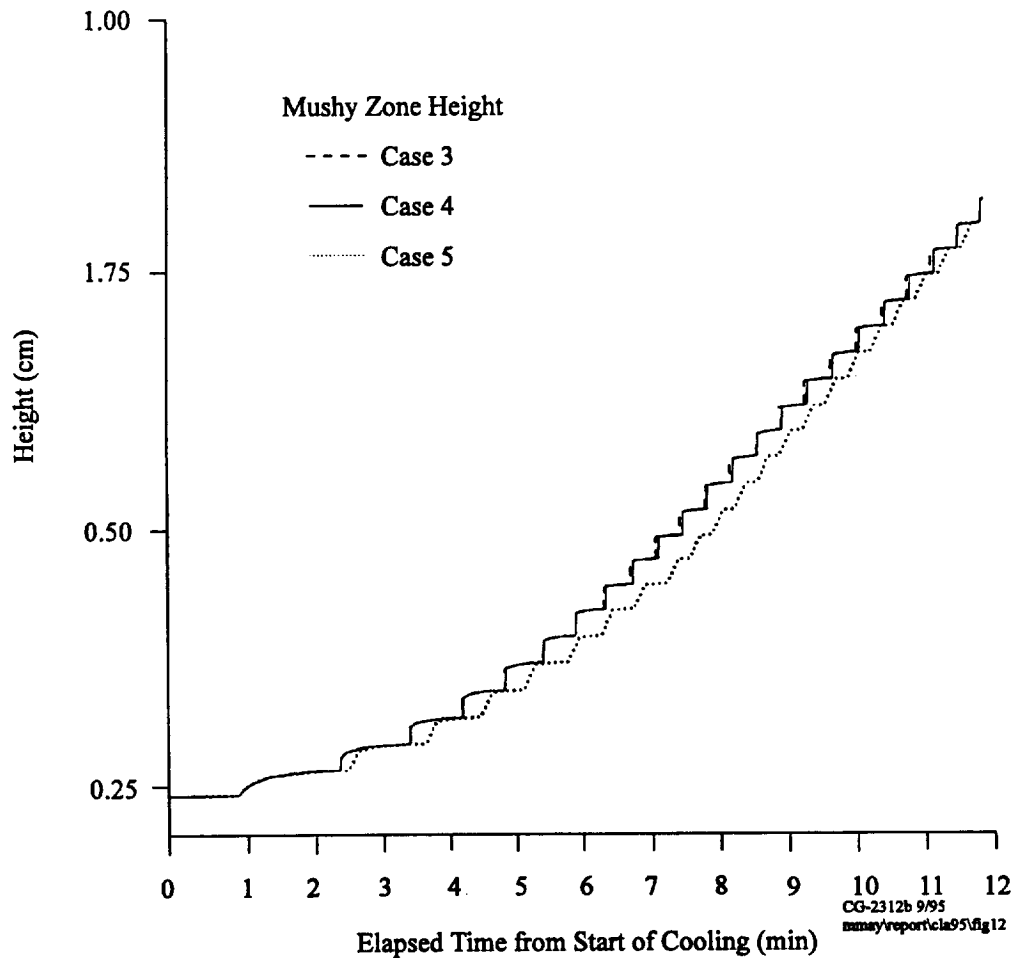


Figure 12. Time Step Dependence (Case 3-5): Mushy Zone Height vs. Time.

The final parameter examined for its effect on the growth of the mushy zone and the solutal field is the third criterion which allows solidification based on the fraction of solid in the neighboring cells. The ground data in Figures 8, 9 and 10 demonstrated that using a neighboring value cut-off of $g_l = .99$ volume fraction of liquid resulted in a close correlation between the predictions and the data. Without this criterion, i.e., assuming equilibrium (which is the same as setting $g_l = 1.0$), the correlation was poor. Figure 13 provides an indication of the sensitivity of the growth rate to the choice of g_l . For $g_l = .95$, the mushy zone height and density inversion height for the early stages of growth are similar, but diverge significantly after two minutes. Therefore, an accurate value of g_l will require extended diffusion dominated growth data. Since one- g growth is limited to approximately two minutes due to convective breakdown, only a microgravity experiment such as on the IML-1 afforded that opportunity.

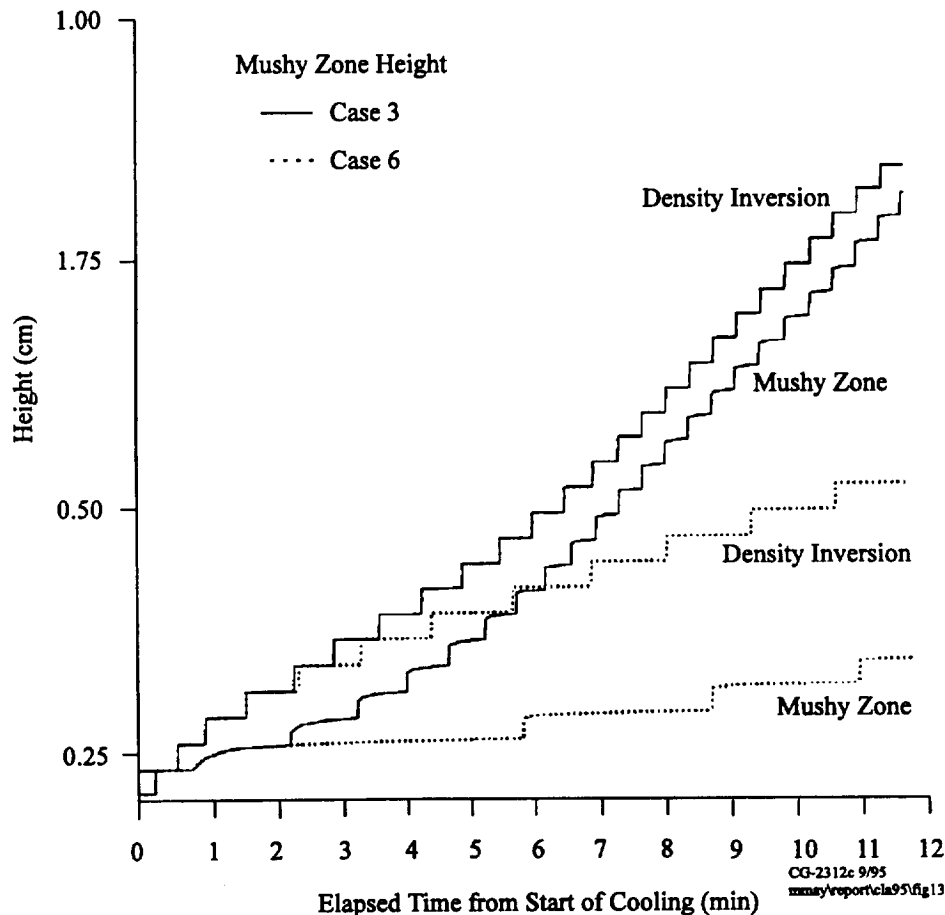


Figure 13. Third Criterion Dependence (Case 3,6).

CAST Linear Stability Model (LSM)

A numerical linear stability model has been developed to support the CAST experiments and the CAST FTM by predicting the marginal states for convective flows occurring during vertical directional solidification. The model predicts the onset of convection for a base state case of a constant solidification growth rate. In doing this, the code also calculates the thermal and solutal fields for the base state case. Flows due to solidification shrinkage are also calculated in the base case.

While the model is currently in the late stages of development, it has been used effectively to predict the onset of convection in theoretical, non-solidification problems. Figure 14 shows a comparison between LSM predictions and theory for the case of an enclosed fluid heated from below. The theoretical values can be found in Chandrasekhar.³²

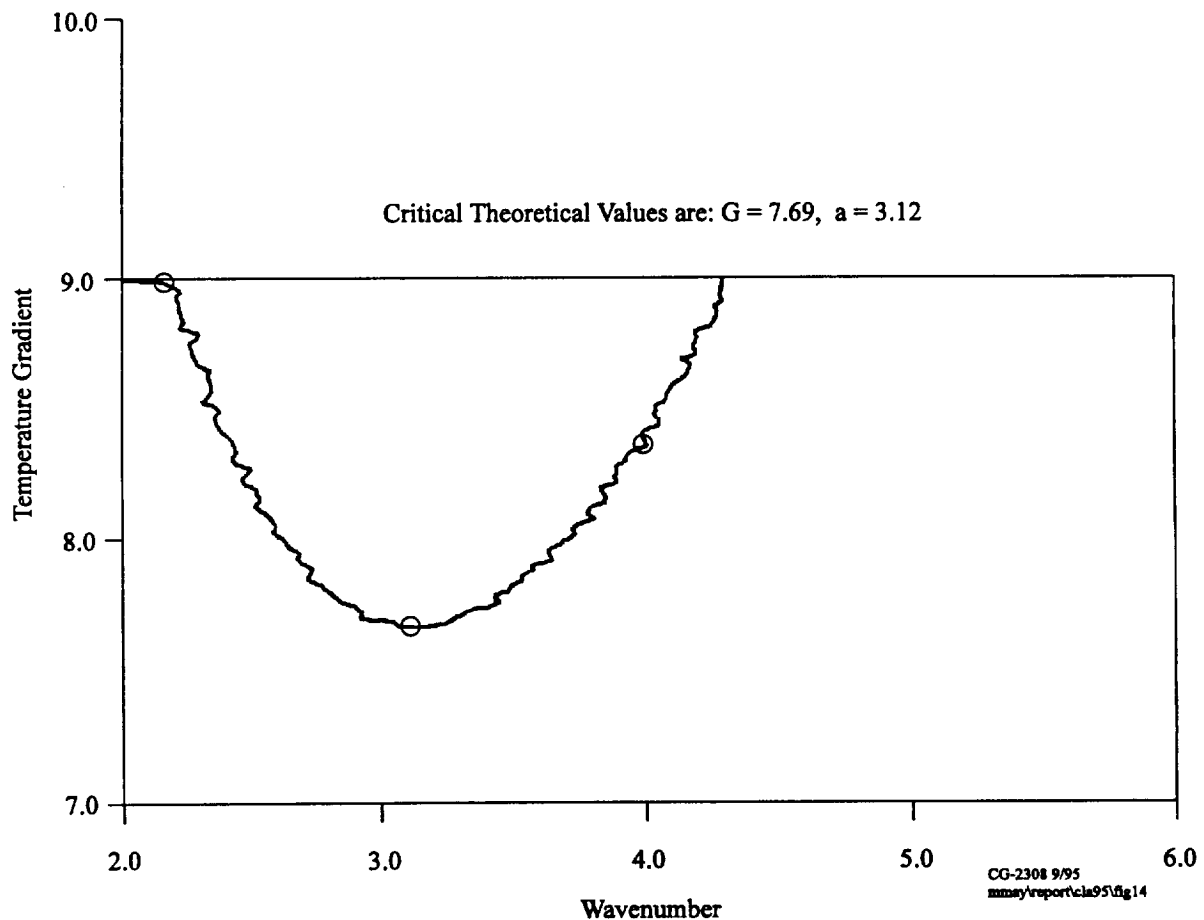


Figure 14. Neutral Stability Curve for Enclosed Fluid Heated from Below Line is from LSM and Symbols are Theoretical Values.

Figure 15 is a comparison between LSM and theory for the case of thermosolutal convection in a fluid between two free surfaces. The LSM predictions match theoretical predictions very closely for both these cases. LSM has also been used with success to predict the stable regimes for the directional solidification of Pb-Sn as in Nandapurkar et al.³³ Figure 16 shows the use of the model to predict the influence of acceleration perturbations on the mushy zone height and the dendrite tip supersaturation ratio.

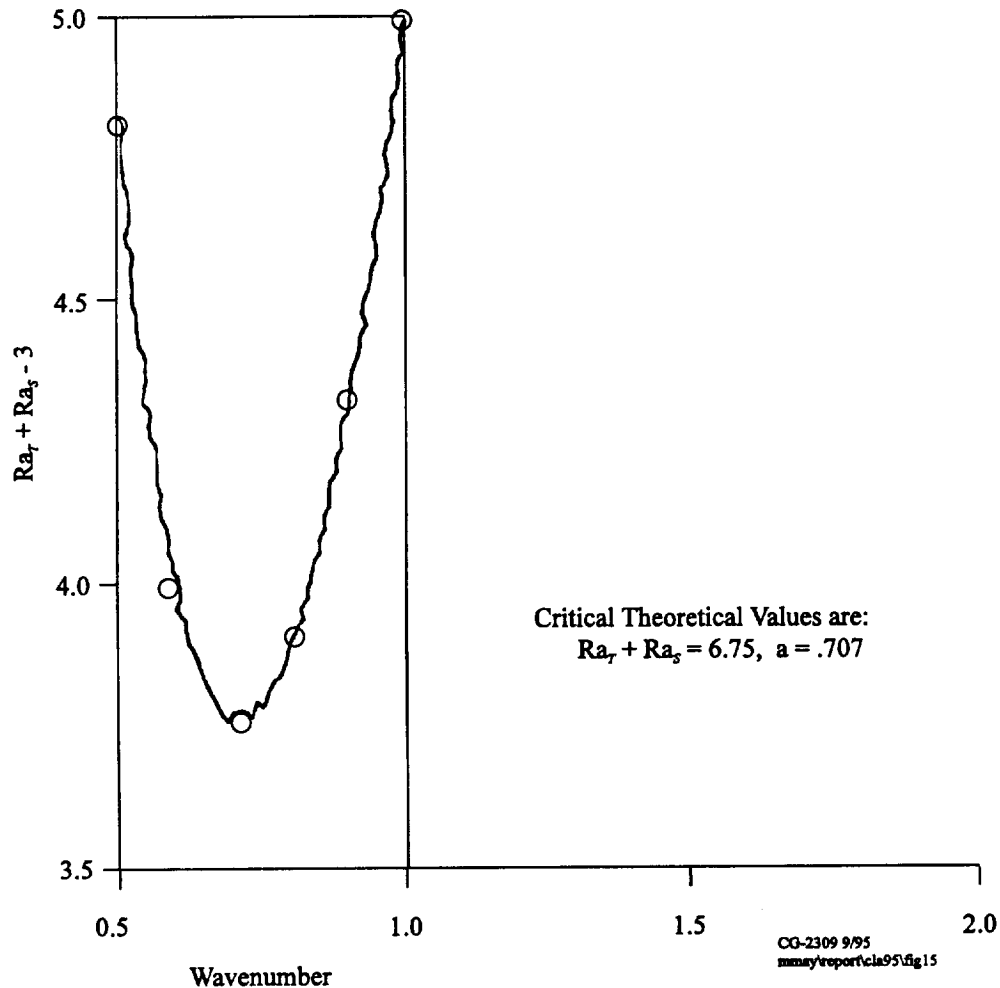


Figure 15. Neutral Stability Curve for Enclosed Fluid Heated from Below. Curve is from LSM and Symbols are Theoretical Values.

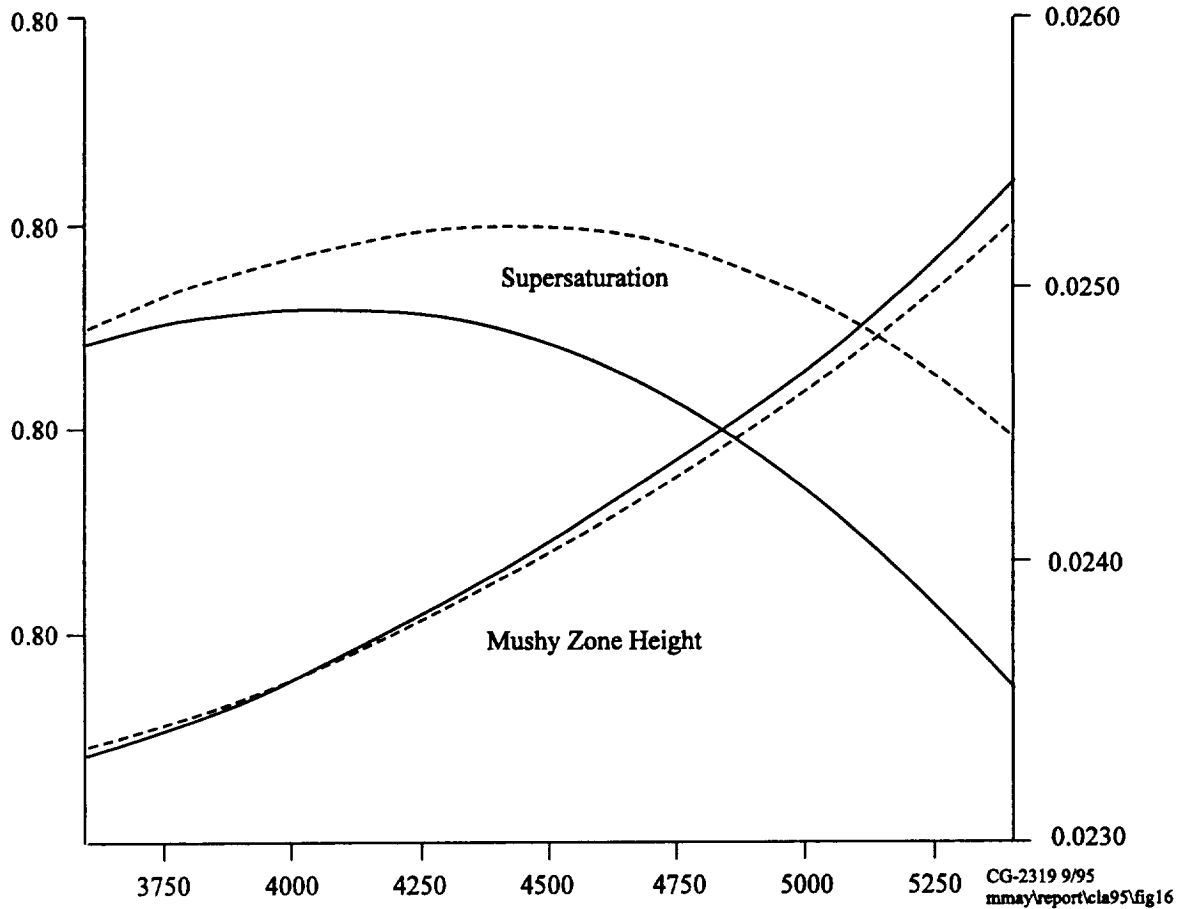


Figure 16. Mushy Zone Height and Supersaturation Ratio After 1 Second Perturbation (—) and Without Perturbation (---) at 3600 Seconds into Solidification.

Numerical Model

The numerical technique used by LSM consists of writing the conservation equations for a two-dimensional, constant solidification velocity process, solving these equations for a nominal base case, rewriting the conservation equations in terms of perturbed quantities, and solving a discretized approximation to the equations to determine if the perturbations are stable. The conservation equations used in LSM are based on the equations used by Nandapurkar³³ but include a provision for calculating contraction flow. The conservation equations written in a coordinate system moving at the growth velocity V are

$$\frac{\partial u_l}{\partial t} - V \frac{\partial u_l}{\partial y} + \frac{1}{g_l} \left(u_l \frac{\partial u_l}{\partial x} + v_l \frac{\partial u_l}{\partial y} \right) = -\frac{g_l}{\rho_0} \frac{\partial P}{\partial x} + v \nabla^2 u_l - \frac{v g_l u_l}{K}$$

$$\frac{\partial v_l}{\partial t} - V \frac{\partial v_l}{\partial y} + \frac{1}{g_l} \left(u_l \frac{\partial v_l}{\partial x} + v_l \frac{\partial v_l}{\partial y} \right) = -\frac{g_l}{\rho_0} \frac{\partial P}{\partial y} + v \nabla^2 v_l - \frac{v g_l u_l}{K} v_l - g_l \frac{\rho}{\rho_0} g_e$$

$$\begin{aligned}
\frac{\partial T}{\partial t} - V \frac{\partial T}{\partial y} + u_l \frac{\partial T}{\partial x} + v_l \frac{\partial T}{\partial y} &= \alpha_T \nabla^2 T - \frac{L}{c_p} \frac{\partial g_l}{\partial t} + v \frac{L}{c_p} \frac{\partial g_l}{\partial y} \\
g_l \frac{\partial C_l}{\partial t} - V g_l \frac{\partial C_l}{\partial y} + u_l \frac{\partial C_l}{\partial x} v_l \frac{\partial C_l}{\partial y} &= \alpha_s \left[\frac{\partial}{\partial x} \left(g_l \frac{\partial C_l}{\partial x} \right) + \frac{\partial}{\partial y} \left(g_l \frac{\partial C_l}{\partial y} \right) \right] \\
&\quad - \frac{(1 - k_p)}{(1 - \gamma)} \frac{\partial g_l}{\partial t} C_l + V \frac{(1 - k_p)}{(1 - \gamma)} \frac{\partial g_l}{\partial y} C_l
\end{aligned}$$

After a base state solution has been obtained, velocity, pressure, temperature, concentration, and density are written as a sum of the base state solution and a perturbation solution to the conservation equations. Nonlinear terms are dropped, and the perturbations are written as the product of a z dependent term, a time exponential term, and a sinusoidal variation in the x -axis as

$$F(x, y, t) = F(y) \exp(\sigma t + i a x)$$

This substitution yields an eighth order non-homogeneous ordinary differential system which can be approximated using finite differences as

$$A \begin{pmatrix} W \\ T \\ C \\ \vdots \\ \vdots \\ \vdots \end{pmatrix} = \sigma B$$

The time decay/growth parameter is set to zero for the marginal case and iterations are performed by calculating the determinant of the finite difference approximation matrix for values of the sinusoidal wavenumber and a selected problem parameter such as the temperature gradient.

The use of a Brinkman extended Darcy form of the momentum equation allows the use of any applicable permeability model for identifying the effects the two-phase mushy zone has on stability. Thus, LSM can be used for two-phase, thermosolutal convective stability predictions as required for the work proposed here.

III. CAST Ground Based Experiment Results

Recent experimental and analytical work by the authors,^{14,16,31,33} has yielded results on the diffusion layer build-up and convective breakdown above a dendritic front. Figure 17³⁰ shows laser interferometer measured concentrations of the diffusion layer over time for the dendritic directional growth of the metal analog, NH_4Cl and H_2O . Data such as these were also used to obtain dendrite tip fluid concentration (Figure 18³⁰) and the supersaturation ratio/tip undercooling (Figure 19³⁰). The time over which these data can be taken is limited to less than two minutes due to the occurrence of convective breakdown of the diffusion layer. The supersaturation ratio³⁴ is analogous to the dimension-less (temperature) supercooling and plays a significant role in the growth process. Studies³⁵ on NH_4Cl dendrites growing into an under-cooled isothermal melt identified three morphological regimes. As supersaturation increased, the primary dendrite orientation changed from $\langle 100 \rangle$ to splitting of the tip with $\langle 100 \rangle$ secondary arms, to $\langle 110 \rangle$ to $\langle 111 \rangle$. The limitations of convection induced by buoyancy did not permit the authors' ground-based experiments to reach sufficient supersaturation to determine if the same morphological effect occurs during solidification in an imposed gradient. This had been postulated as occurring in an earlier low-gravity SPAR experiment³⁶ but as yet remains unconfirmed. Since a superimposed thermal gradient is normally employed in directional growth of superalloys, this question is highly significant.

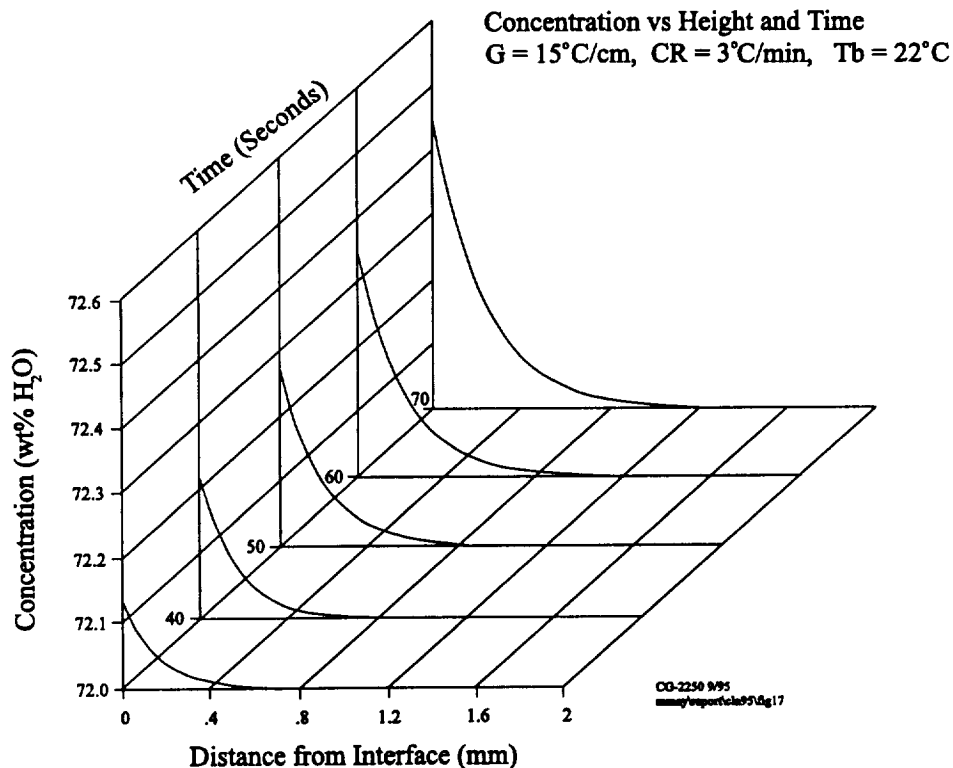


Figure 17. Diffusion Layer Build-up for Cooling Rate = $3^\circ\text{C}/\text{min}$.

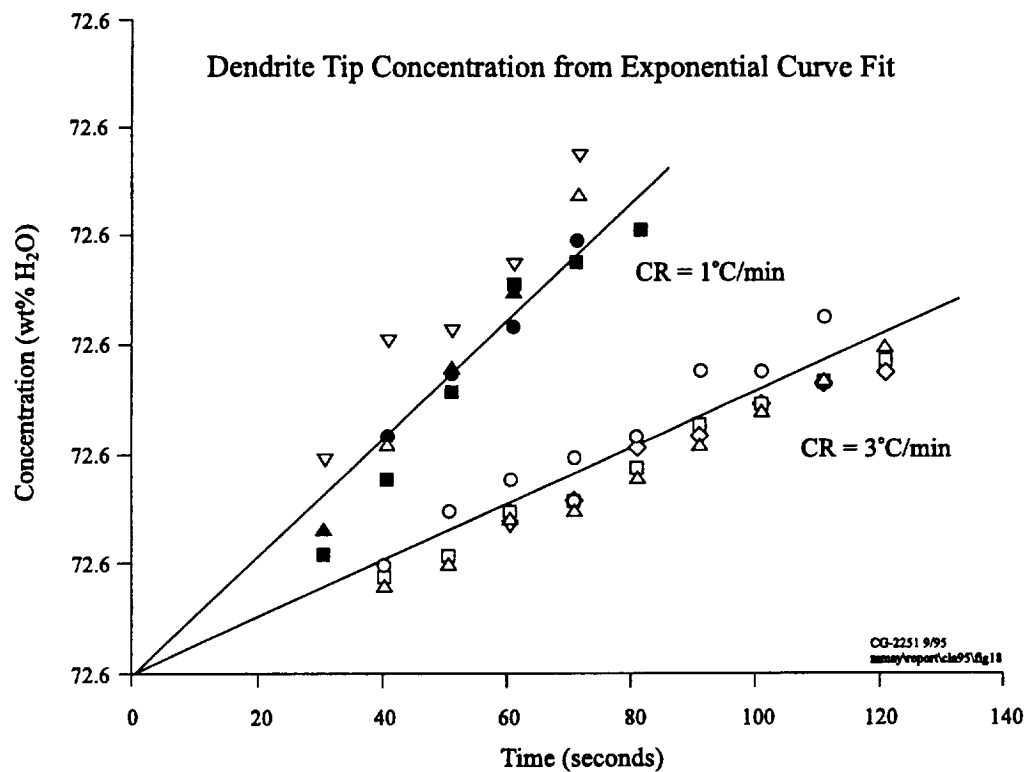


Figure 18. Time Dependence of Dendrite Tip Concentration.

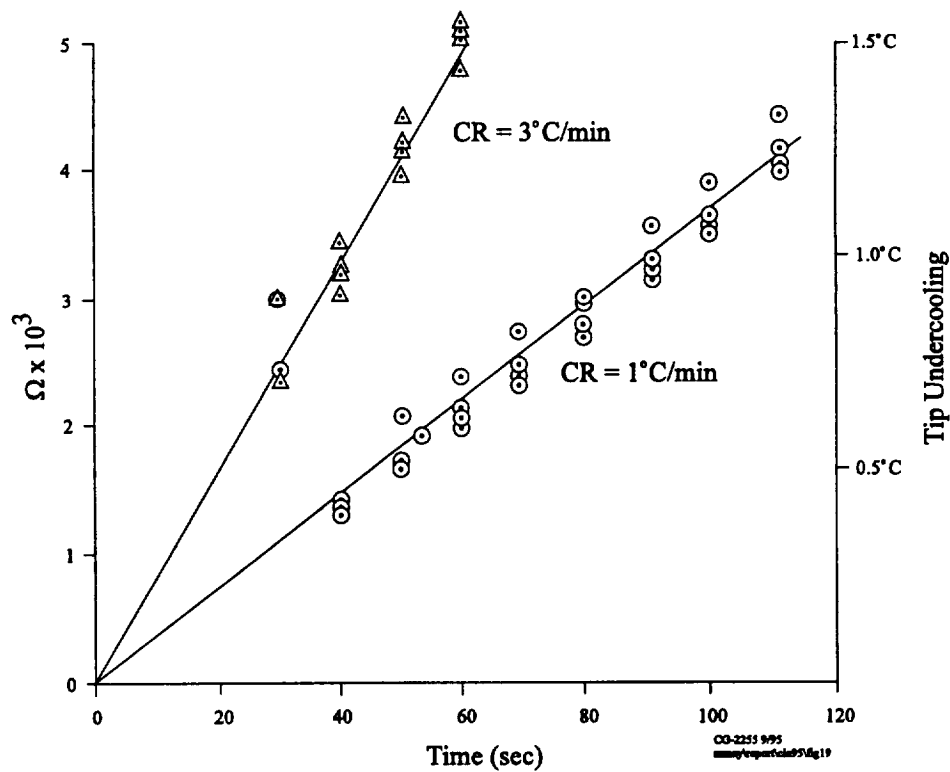


Figure 19. Supersaturation Ratio and Tip Undercooling as a Function of Time.

Unfortunately, in one- g the diffusion layer breakdown begins within several minutes of the start of solidification. Extensive pluming occurs shortly after the ordered breakdown, followed by macroconvection within the bulk liquid. The influence of these flow regimes on the interface growth and the diffusion layer can be seen in Figure 20.

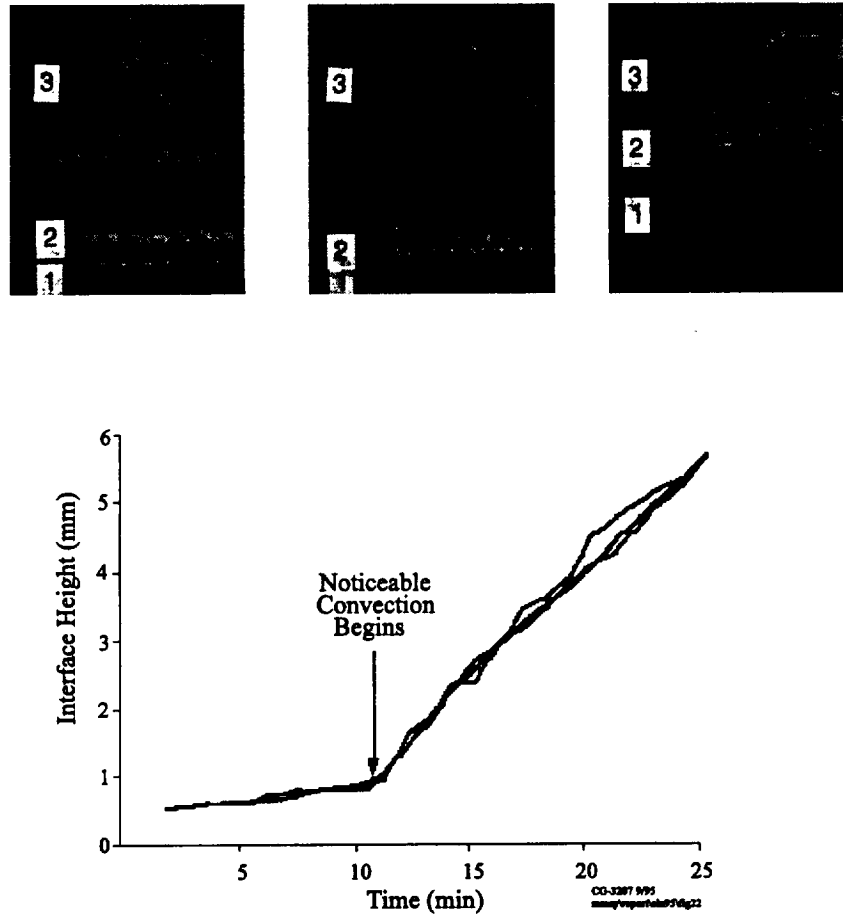


Figure 20. The Interface Height as a Function of Time with COPS photographs at (a) 2 minutes, (b) 8 minutes, and (c) 15 minutes. Region 1 is the mushy zone, 2 is the diffusion layer, and 3 is the bulk fluid.

There appears to be three segments to the data; an almost flat initial section, a small rise over intermediate times, and a significant rise at the longer times. These will be called stage one, two, and three in further discussions. Growth rates were determined from curve fits to the data in stages two and three. There is approximately an order of magnitude increase in the growth rates as the system transitions from stage two to stage three. (Growth in stage one is not included on these plots, since it was too low to be accurately measured with the present system. It was estimated to be in the 10^{-2} cm/h range for all experiments.)

The onset of stage two growth is associated with the initiation of cellular convective breakdown of the diffusion layer and centered around the density inversion.^{14,31} Rayleigh

numbers at the onset of stage two (the critical Rayleigh number for cellular breakdown) were calculated using the $\text{NH}_4\text{Cl-H}_2\text{O}$ property values in Table 1. The inverted layer heights (H_m) at the beginning of stage two were obtained from the optical data measurements. The temperature difference (ΔT) across the inverted layer was obtained from the calibration temperature runs. The weight percent concentration difference (ΔC) was calculated assuming that the null was at the bulk concentration (a good approximation) and that the concentration at the cuvette bottom was dictated by the phase diagram value based upon the lower internal wall temperature. Attempts were made to correlate the breakdown with various parameters, such as the layer height above the mushy zone ($H_m - H_z$) rather than the inverted layer height, (H_m), alone. These were unsuccessful. The stage two critical Rayleigh number is shown plotted in Figure 21 as a function of the mushy zone height, H_z .

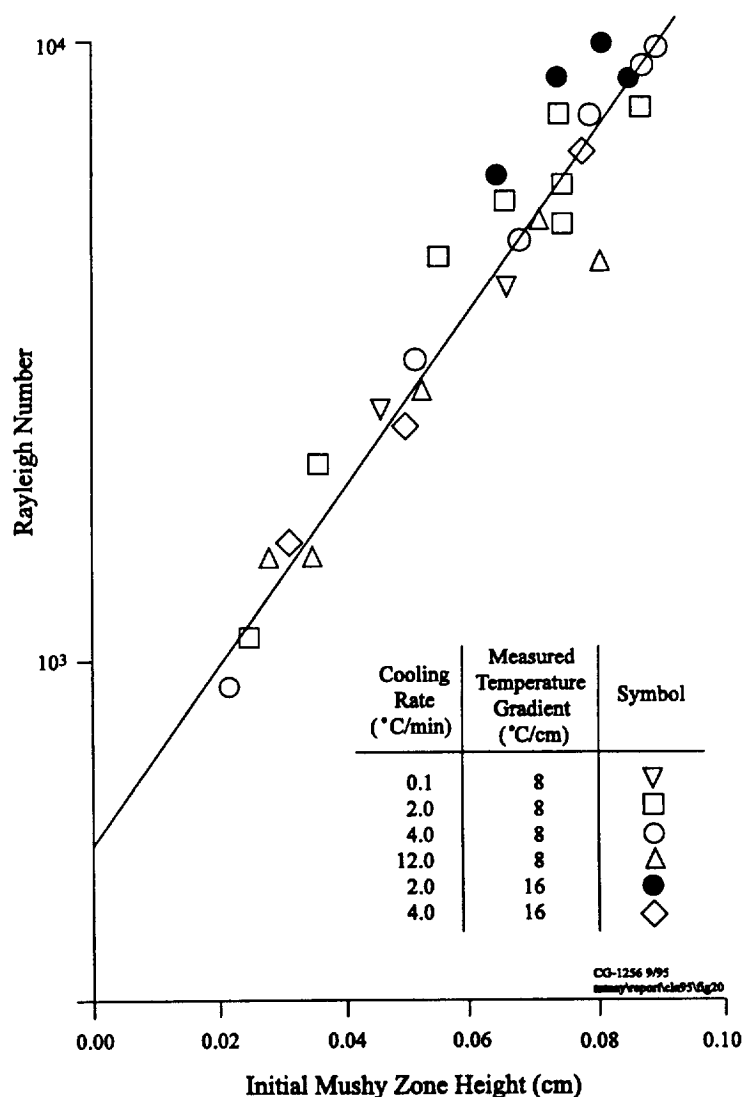


Figure 21. Critical Rayleigh Number Variation with Initial Height of the Mushy Zone.

During stage two growth, the diffusion layer shrinks and maintains a consistent (though lower) height above the slowly growing front. Columns of liquid can be seen rising from this layer. Another stage then eventually occurs. The flow increases dramatically and the growth rate of the dendrites increases an order of magnitude over that of the previous stage. Since there appeared to be a definite transition between stages two and three, Rayleigh numbers were also calculated for the transition using the associated inverted layer height (H_m), mushy zone height (H_z), and the properties given previously. The second critical Rayleigh number also has a dependence on the mushy zone height, although the functional form is not fitted as well as for the onset of stage two.

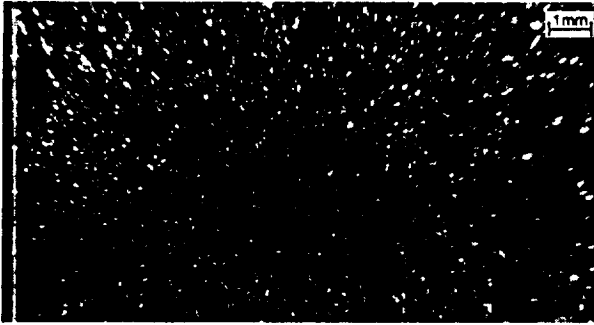
If a regression analysis is applied to the data for the functional form given in the equation, one obtains

$$\begin{aligned} Ra_c &= Ra_0 e(P_m H_z) \\ \text{or for stage two,} \quad Ra_c &= (980 \pm 160)e(57.2 \pm 3.8)H_z \\ \text{and for stage three,} \quad Ra_c &= (1.2 \times 10^3 \pm 3.7 \times 10^3)e(13.7 \pm 4.4)H_z \end{aligned}$$

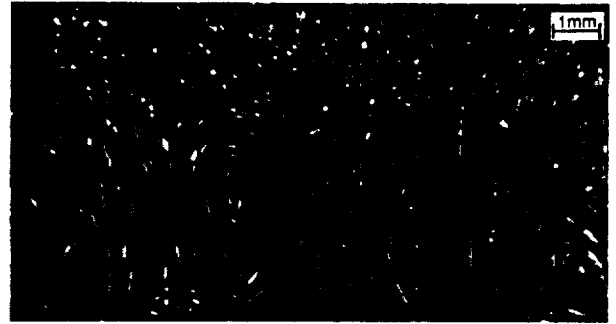
where Ra_0 is the intercept at $H_z = 0$ and P_m is the slope and represents a porosity factor. For stage two, the value obtained with these new additional data points adjusts the previous critical Rayleigh number¹⁴ to a value closer to that reported in earlier literature.³⁷ The choice of the exponential fit for stage two is based upon goodness of fit. The same functional form was chosen for stage three merely to provide consistency.

For negligibly small mushy zone heights, the cellular stage two flow begins at a lower Rayleigh number than the stage three flow. At a mushy zone height of 0.06 cm, however, the curves intersect indicating that stage three flow occurs prior to stage two flow for all greater mushy zone heights. This was substantiated by additional laboratory experiments in which the initial (starting) mushy zone was established at a height greater than 0.06 cm and a shadowgraph optical arm was added to the configuration. In these experiments, the cellular (stage two) flow is not observed and stage three flow occurs immediately, along with the associated stage three increase in growth rate.

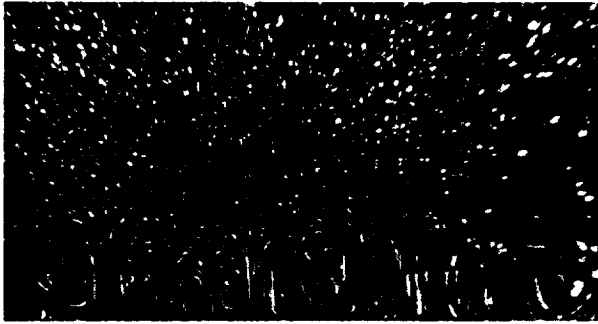
Figure 22 presents a sequence of neutrally buoyant particle tracking photographs (magnified to isolate the diffusion layer) which show the intermediate stages of flow, i.e., between the stage two initial convective breakdown of the diffusion layer and the long term stage three effects which eventually lead to chimney formation. Figure 22(a) is at the very onset of convection, the cellular structure is barely visible in the photo. The upward/downward flows in the small cells create depressions in the interface. In Figure 22(b) the cellular flow structure is well developed and the vortical patterns are easily discerned. After several minutes the cells develop into a multiple level system with sufficient buoyancy through a combination of solutal and thermal effects to evolve from a vortical pattern to a full-fledged plume. Once plumbing is established, the occurrence of jetting chimneys and channels is a natural ramification. It is noteworthy that the presence of a superposed positive temperature gradient significantly modifies the physical behavior being observed. This accounts for the differences between these observations and others typically seen in the literature where the upper bound on the diffusion layer is a constant temperature fluid.²⁴ The latter case promotes the classic salt fingering but this does not occur in the same fashion in a system with a superposed positive gradient.



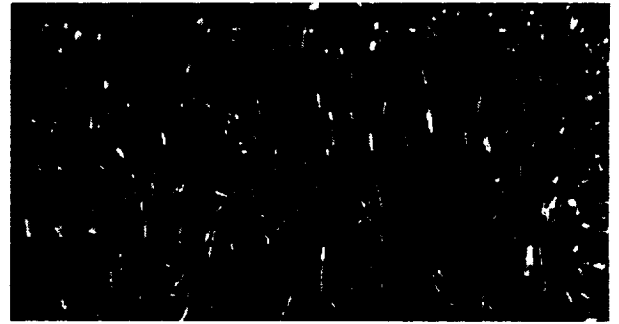
(a)



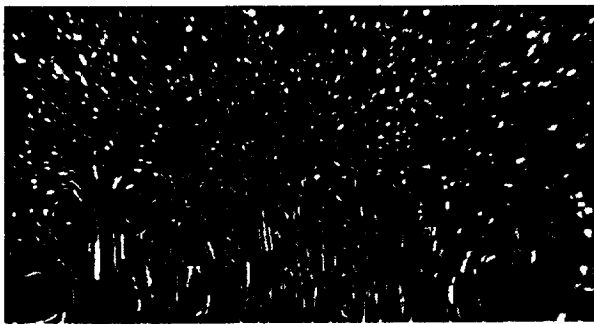
(d)



(b)



(e)



(c)



(f)

Figure 22. Particle Tracking Photographs Illustrating the Stages of Flow During Dendritic Solidification, (a) 90 Seconds, (b) 106 Seconds, (c) 120 Seconds, (d) 180 Seconds, (e) 210 Seconds and (f) 240 Seconds.

In addition to studies of bulk -convective flow effects on the overall mushy zone height, individual dendrite growth rates were obtained as a function of flow direction³⁸ using particle tracking. These are shown in Figure 23 (the dendritic front average growth rates are also noted on the plots). In all cases, the individual growth rate fluctuates around the average growth rate, being either faster or slower depending on the actual flow direction. When the flow is upward ($+90^\circ$ on the plots) along the growth direction of the dendrite, the growth rate is decreased to a value below the average. As the flow direction rotates, the growth rate slowly increases, reaching a maximum when the flow nears a direction opposite to that of growth (-90°). Interestingly enough, the maximum in growth rate does not appear to occur when the flow direction and dendrite are exactly anti-parallel.

This dependence of growth rate on fluid flow direction is a result of the relative influence of the thermal and solutal diffusivities. The upward flowing fluid is cold, which should encourage growth and yet the growth slows significantly. In contrast, the downward flowing fluid is warm, which should inhibit growth, and yet the dendrite grows more rapidly. On the other hand, the upward flowing fluid is depleted of solute and therefore growth would be expected to slow, whereas the downward fluid is the bulk concentration and therefore growth would be expected to increase when it reaches the dendrite. Hence the growth is being dominated by concentration rather than heat transfer effects.

These results illustrate the significance of relative diffusion rates in the solidification process. The difference in thermal (D_T) and solutal (D_S) diffusion rates (in this case $D_T/D_S \sim 70$) contributes not only to thermosolutal convection but also to the local dendrite growth conditions. Due to the relatively high thermal diffusivity, the cold, ascending, solute rich liquid equilibrates to the higher temperatures while retaining its high solute concentration. Hence the liquid in this local region drops even further below the saturation concentration and is less favorable for dendrite growth. Similarly, the warm descending, low solute concentration fluid cools as it drops toward the interface and becomes super-saturated. Consequently, it is more favorable for dendrite growth, and the growth rate in the vicinity of this flow increases.

The local dendrite growth conditions are governed by the combined effects of convective and diffusive heat and mass transfer. The disparity in thermal and solutal diffusivities not only creates an impetus for convective motion, but also directly influences dendritic growth by altering the local solute supersaturation. The local fluid motion, thus, does not independently determine the local dendrite growth rates.

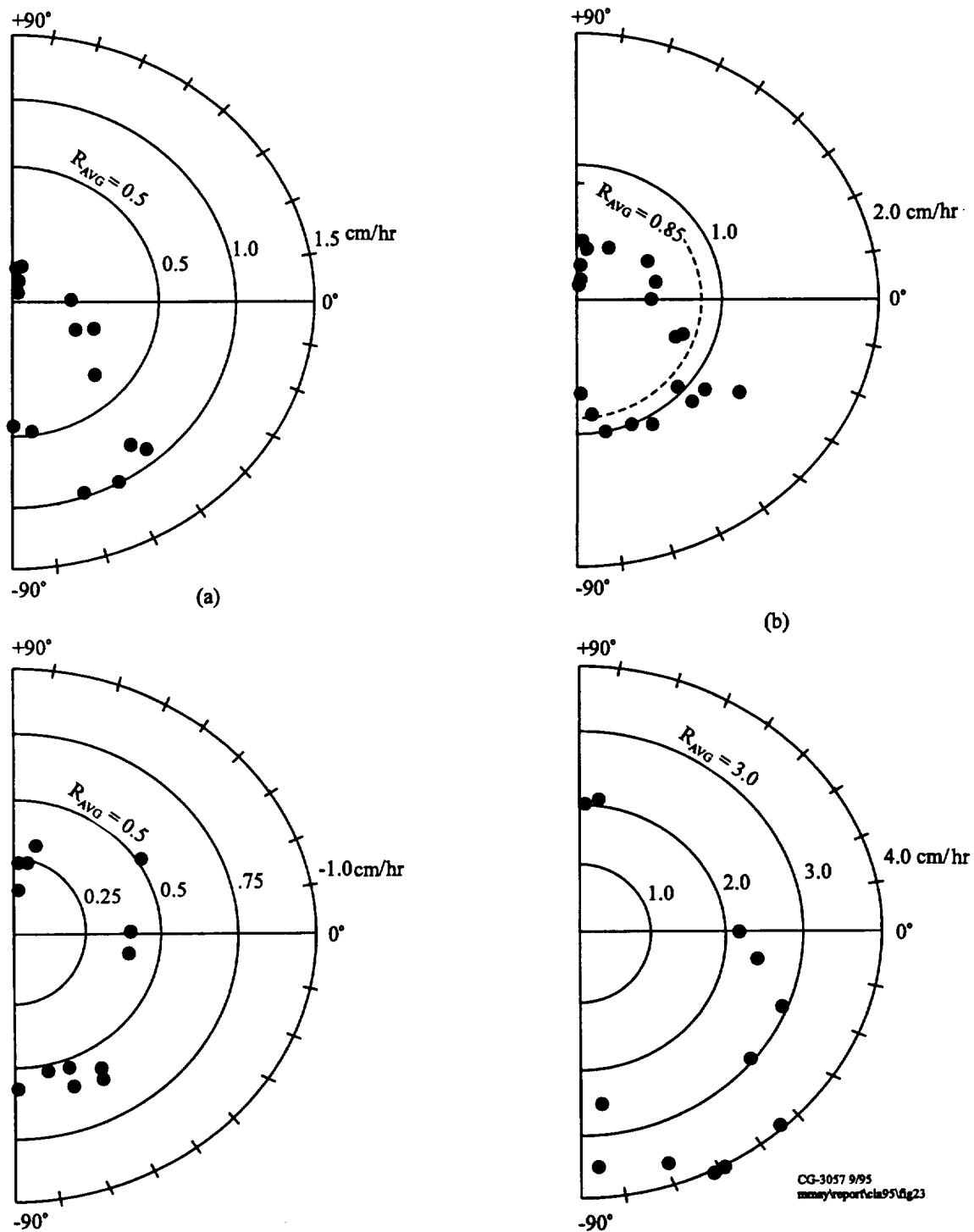


Figure 23. Growth rates of individual dendrites as a function of fluid flow direction (+90 means flow is in the growth direction; -90 means flow is opposite to the growth direction.)

IV. CAST IML-1 Experiment Description

The CAST experiment flew in the Fluids Experiment System (FES) on the International Microgravity Laboratory-1.

Experimental Procedure

A 28.5 wt% $\text{NH}_4\text{Cl-H}_2\text{O}$ solution was sealed in an optical quality quartz cuvette with two millimeter wall thicknesses and inner dimensions of 25 by 16 by 8 millimeters. The cuvette had a double contraction expansion tube which enabled the solution to expand and contract without either damaging the cuvette or allowing bubbles and free surface effects. Thermoelectric devices (TED's) placed at the top and bottom (16mm \times 8mm) surfaces provided the capability for controlled heating and cooling. When configured for flight, the cuvette assembly was located in a purged and sealed container, called the CAST Science Module (CSM), with double walled optical quartz windows. Temperatures were monitored on the external walls of the cuvette itself and on the heat sinks for the TED's. Prior to the flight, a series of calibration runs with internal thermocouples was conducted to obtain temperature profiles and isotherm translation rates (ITR) within the cuvette during standard ground-based runs. They were also used to establish the correct relationship between externally measured and actual internal fluid temperatures and for comparison with the external thermistor data for computational model validation. Temperature control during the flight was provided by the Fluids Experiment System (FES). An identical control system (GCEL) was used at the Marshall Space Flight Center (MSFC) for the ground-based experiments.

The FES is an optical diagnostic facility which provides the capability for conducting experiments on transparent fluid systems in microgravity. Programmable heating and cooling are accomplished through TED's. While the primary data from the experiments are holograms of the optical cuvette and fluid during a run, temperature and gravity level are also monitored and a Schlieren downlink video enables the researcher to view the experiment real-time. Astronauts operate the facility while in orbit and provide hands-on capability for modifying experiment parameters.

Since it was necessary to run the flight experiment continually over a 40 hour time period, two CSM's were used and alternated in the FES. Therefore, prior to each of the ground and flight experiments, it was necessary to re-solutionize the previously solidified $\text{NH}_4\text{Cl-H}_2\text{O}$ material by attaching the CSM to a premelt controller, heating to 30°C (the saturation temperature is 25.04°C) and manually shaking the CSM at repetitive intervals. On earth the undissolved dendrites sank to the bottom (cooling surface) of the cuvette. In micro-gravity the astronauts developed a maneuver to drive the remaining solid to the bottom of the cuvette after shaking. When only a small (less than 0.1 mm) layer of dendrites remained, heating was discontinued and the cuvette assembly was placed into either the FES or the GCEL for operation of the experiment timelines. The presence of a small amount of solid at the start of the experiment runs was a requirement to eliminate the extensive undercooling that can occur in the $\text{NH}_4\text{Cl-H}_2\text{O}$ system. Although the use of this technique precluded an absolute knowledge of the well mixed remaining liquid, the fraction

of solid which was necessary was so small as to permit the 28.5% NH_4Cl concentration to be assumed for all analyses. In addition, since the optical analyses employs changes in concentration rather than absolute concentration, very little inaccuracy was introduced into the final data. In fact, the percent error involved was two orders of magnitude less than the expected experimental error from other sources.

The protocol for the experiments was as follows: The CSM was installed into the control system. The top and bottom TED's were set to provide a pre-selected temperature gradient. The gradient was allowed to equilibrate for twenty-five minutes, a requirement determined from preliminary thermocouple and optical measurements in fully instrumented cuvettes. A single exposure hologram was then taken. Bridgman directional solidification was then accomplished by simultaneously ramping the TED's at a linear rate. Single and double exposure holograms were taken at selected intervals during the solidification. Table 3 shows the temperature gradients, cooling rates and calculated isotherm translation rates (ITRs) for the experiment runs. Two duplicate runs (No. 1 and No. 6) were conducted which were conditions duplicating the most extensively studied ground-based case. The remaining runs were conducted at one of three pre-selected ITRs. Both the microgravity ($10^{-5}g_e$) and one-gravity experiments were performed using the same cuvette/solidification apparatus and experiment conditions. It should be noted that the fraction of solid at the cold end during a run never exceeded 90% since the lowest temperature in any of the experiments never reached the eutectic temperature. Eight of the flight experiments were successfully completed and produced a sufficient number of satisfactory holograms for analysis.

In addition to the holographic snapshots, the progress of the growth front and the diffusion of the water-rich layer was monitored real-time using a classical schlieren optical system. Furthermore, real-time thermistor data permitted the monitoring of the temperature gradient and cooling rates. This permitted comparison of the thermal data between the flight and ground-based runs and analytical model predictions.

V. CAST Flight Experiment Results

After the experiments were completed, the holograms were developed at MSFC and reconstructed at The University of Tennessee Space Institute. Examination of the reconstructed holograms using an interferometer²¹ and a confocal optical processing system¹³ allowed determination of the uniformity of the concentration and temperature fields.

Growth Rate Effects

Growth front height as a function of time was obtained for each of the eight runs from the reconstructed ground-based and flight holograms.³⁹ Figure 24 shows the data for run # 4 at times for which satisfactory holograms were available. Growth rates were extracted from linear curve fits starting with the time at which the holographic data indicated the dendritic front was uniformly distributed across the cuvette. For comparison purposes, the growth rate of the flight experiment dendritic front for the eight experiments is shown plotted versus the growth rate of the ground-based dendritic front in Figure 25. The ground-based dendritic growth rates are lower than the flight growth rates for seven of the eight runs analyzed, being approximately one-half of the flight rate for six of the runs. The experiment with the slowest cooling rate (4.5°C/hr) does not follow this trend. It is probable that this anomaly (and the fact that the other slow cooling rate flight experiment does not quite follow the trend) is due to the microgravity growth front not yet having reached its maximum rate.

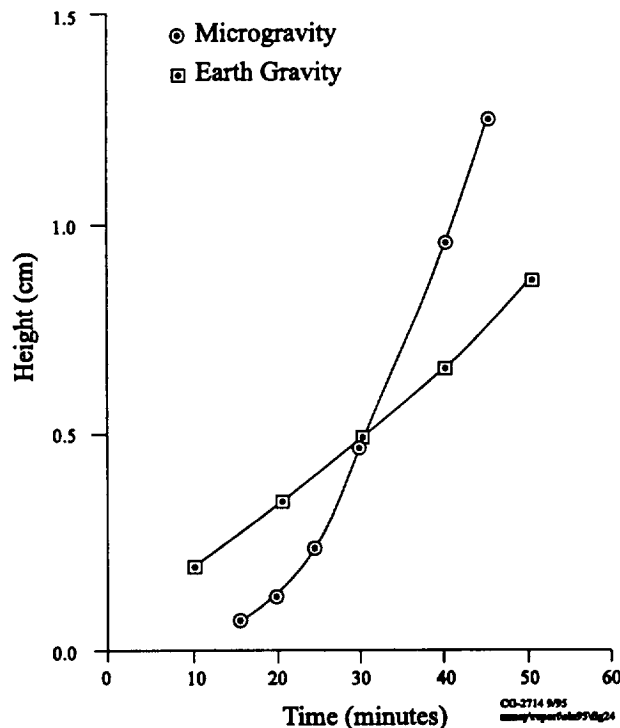


Figure 24. Growth front height as a function of time for microgravity and ground-based experiment (run 4, holographic data).

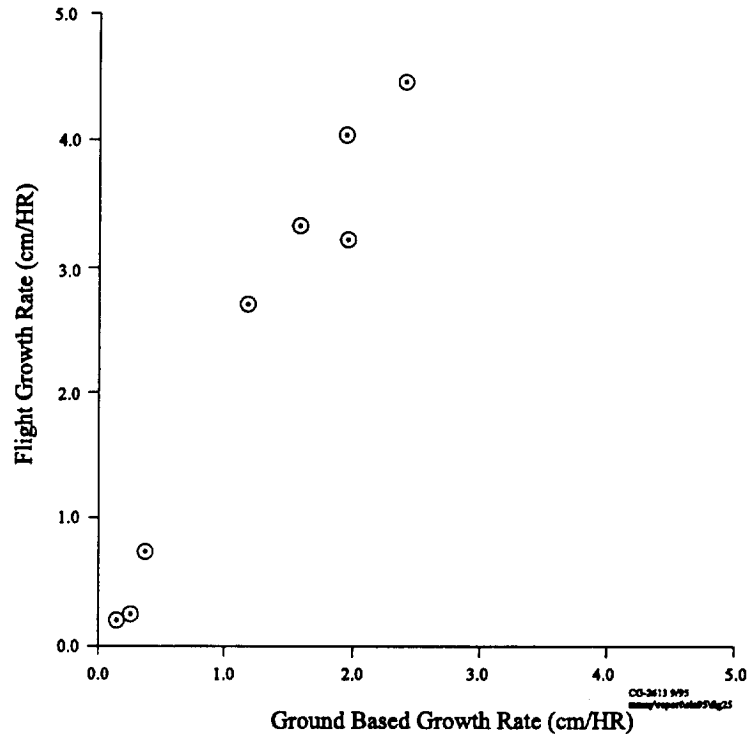
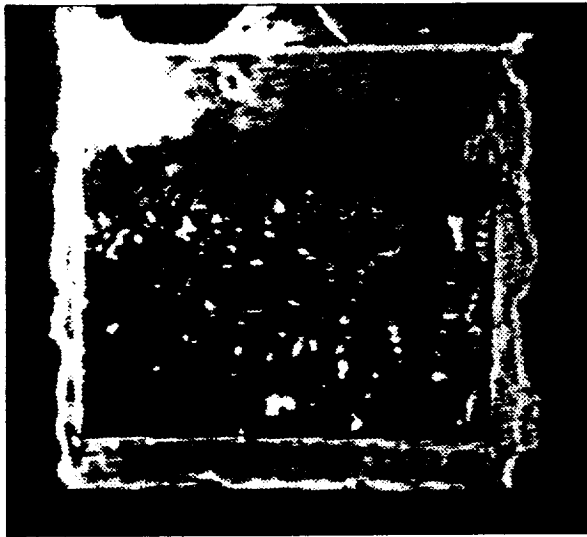


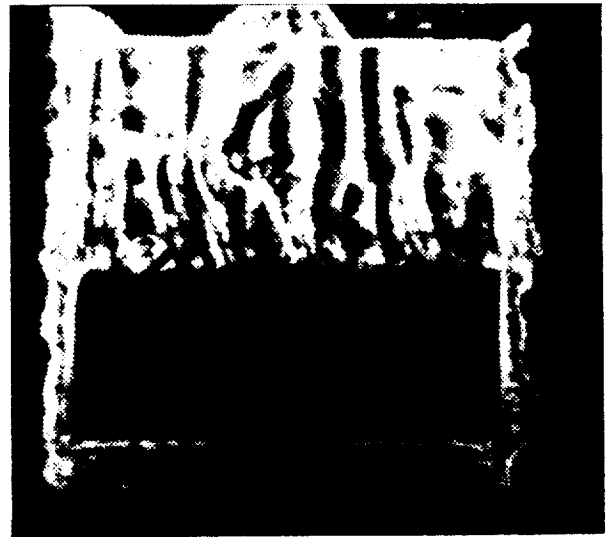
Figure 25. Growth rate of flight experiment dendritic front versus growth rate of ground-based experiment dendritic front (identical solidification parameters).

Permeability Effects

Another significant difference between the ground-based and the flight dendritic growth is visually apparent in Figure 26 which shows reconstructed single exposure holograms of the growth fronts at the end of run No. 4. The mushy zone is too dense to be transparent in the ground-based experiment whereas it is transparent in the flight experiment, and individual dendrites can be distinguished. (This was noticed initially during the IML flight when one of the astronauts held the CAST Science Module up to the video camera for viewing. It was confirmed later when the flight holograms were developed and reconstructed.) This demonstrates the role that the buoyancy mass transport mechanism plays in influencing the concentration of the interdendritic liquid within the mushy zone and the volume fraction of solid formed. As the extent of convection increases, the NH_4Cl concentration of the interdendritic fluid increases due to the movement of higher solvent concentration fluid into the mushy zone. This increases the solvent concentration adjacent to the dendrites. Since the ratio D_T/D_S of $\text{NH}_4\text{Cl}-\text{H}_2\text{O}$ is ~ 70 the convected fluid cools and the excess NH_4Cl solidifies, producing a higher volume fraction of solid and a more dense mushy zone.



(a)



mms\report\cia95\fig26

(b)

Figure 26. Reconstructed holography views of dendritic front at end of run 4 (a) in microgravity and (b) on earth.

Diffusion Layer Effects

The height of the two-phase region and the height of the inverted density region were measured and used to obtain the extent of the diffusion layer.⁴⁰ Since the flight experiment did not provide sufficient time resolution to monitor the build-up of the layer (this was to be obtained from a second flight), the layer width was measured after it reached a consistent thickness.

Figure 27 presents the flight and ground-based diffusion layer widths as a function of the applied cooling rates. The flight widths follow an inverse relationship to the cooling rates as would be expected since cooling rate divided by gradient is equivalent to growth rate. In fact, the widths fall within the theoretical calculated values of $2D/V$, indicated on the figure for the experimental conditions (assuming $D = 2.302 \times 10^{-5} \text{cm}^2/\text{sec}$ and the temperature gradients range between 5 C/cm and 15 C/cm).

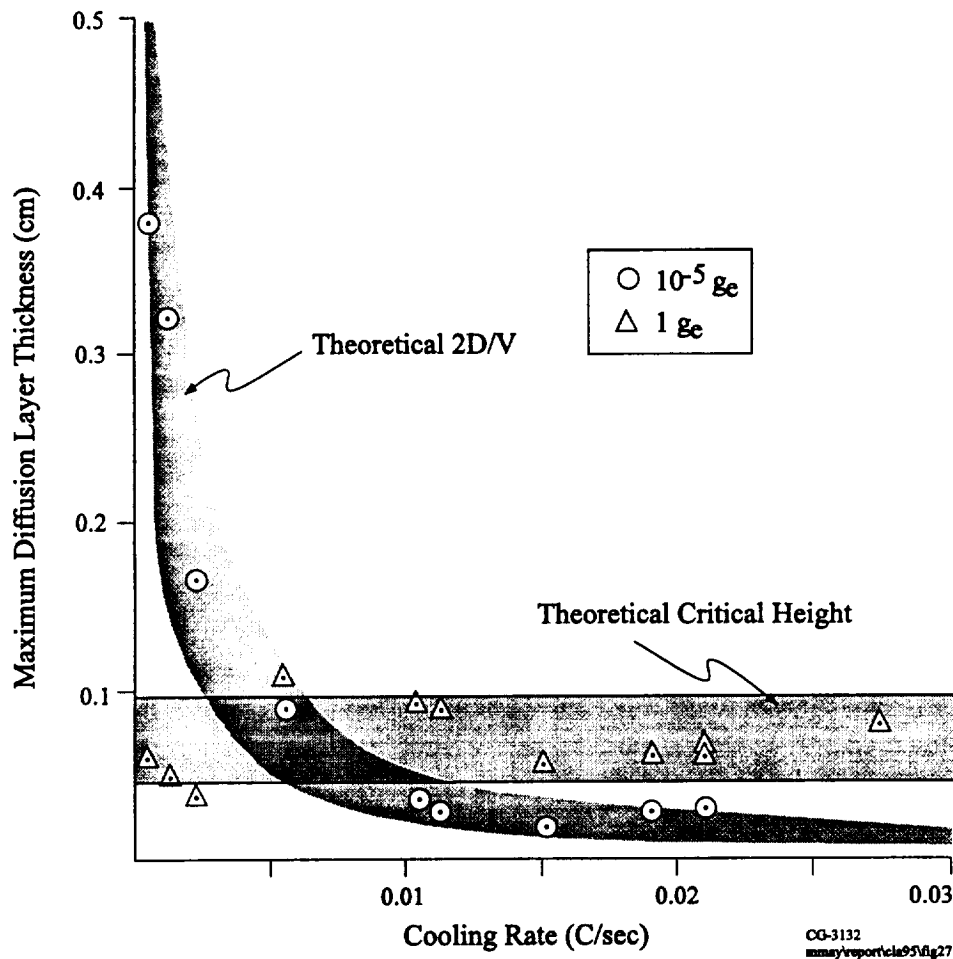


Figure 27. Flight and Ground-based Diffusion Layer Widths as a Function of Cooling Rate.

The ground-based data, however, do not show any trend with cooling rate, in fact they appear to be independent of the cooling rate. The results at the lower cooling rates can be explained by the breakdown phenomena referred to earlier which occurs when the layer reaches a height dictated by the critical Rayleigh number.³¹ The range of theoretical calculated critical heights for breakdown are also shown on the figure for the experimental conditions in one gravity. (These values exist over a range of heights due to differences in concentration across the layer with each experiment.) For the experiments in which the critical height is lower than $2 D/V$, the layer becomes unstable and breaks down before reaching its theoretical maximum. As a result, the lower cooling rate experiments show a smaller than theoretically expected layer width.

The faster cooling rate results could be due to one of the following phenomena: long solutal transients, end effects, or an increasing effective diffusivity. Long solutal transients are very unlikely since this effect would occur over a different time scale, that of hours and days, from the experiments which lasted for approximately twenty minutes for the

fast cooling rate runs. Similarly, since the experiments were halted before reaching the top quarter of the container, end effects would not be a factor.

An increase in effective diffusivity can be discussed in light of more detailed examination of the diffusion layer formation. Figure 28 shows a typical diffusion layer concentration profile measured at five times during the growth of the layer. Assuming an exponential form to the profiles, a D/V curvefit value can be determined at each time. If the growth rate is also assumed constant, the change in diffusivity can be calculated and found to increase with time for four experiment cases. If the growth rate is assumed to increase, this calculated diffusivity would decrease. However, if the growth rate decreases, the diffusivity would once again be found to increase. Hence a reduction in growth rate, possibly due to constitutional effects, would increase the effective diffusivity and result in a larger diffusion layer. Microconvection^{19,20} could also be a contributor to the diffusivity increase, causing boundary layer flows to occur along the dendrite stalks as a result of the light solute rejection. Unfortunately, the experimental apparatus was not designed to resolve either of these two possible contributors to the effective diffusivity and therefore at this time a conclusion cannot be made as to the cause of this phenomena.

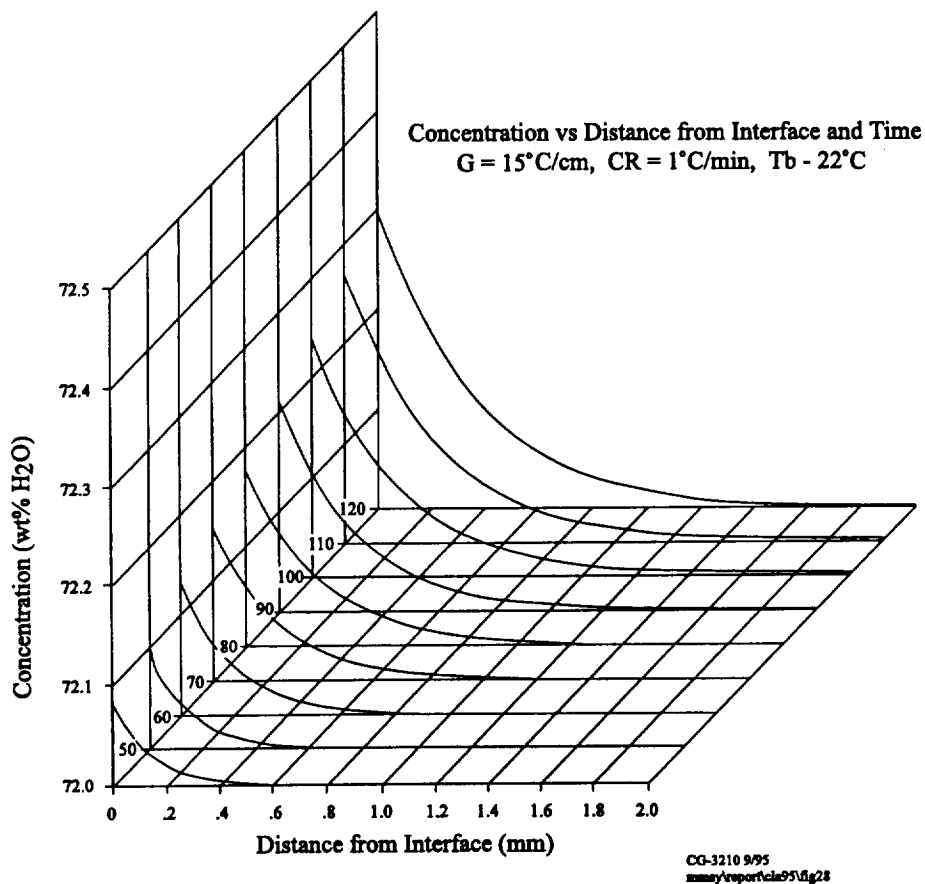


Figure 28. Typical Diffusion Layer Concentration Profile Shown Over Time Prior to Convective Breakdown.

Arm Spacing Effects

Although the CAST flight experiment was not designed to obtain secondary arm spacings, several of the flight experiment runs produced holograms of sufficient quality to obtain data. (It should be kept in mind, however, that since the experiment was not designed to obtain this data, it should only be used to suggest qualitative trends and not develop absolute quantitative information.) Figure 29 presents the data for both the flight and ground-based experiments on a ln/ln scale of secondary arm spacing versus local solidification time. (Local solidification time was selected as the most accurate representation. It was determined by measuring the distance of the dendrite arm from the tip and calculating time from the growth rate.) Applying the relationship

$$d_s = bt_s^n \quad (2)$$

where d_s is secondary arm spacing, b is a constant, and t_s is local solidification time. The exponent n is determined to be 0.32 for the flight experiment and 0.16 for the ground-based experiment. Although there is considerable data scatter, this is a significant difference. The lower value of n for the ground-based experiment has been reproduced in two other series of experiments conducted on two different solidification systems in the CAST laboratory. Therefore, it appears that the flight experiment follows the predicted relationship for secondary arm spacings as a function of local solidification time whereas the ground-based experiment does not.

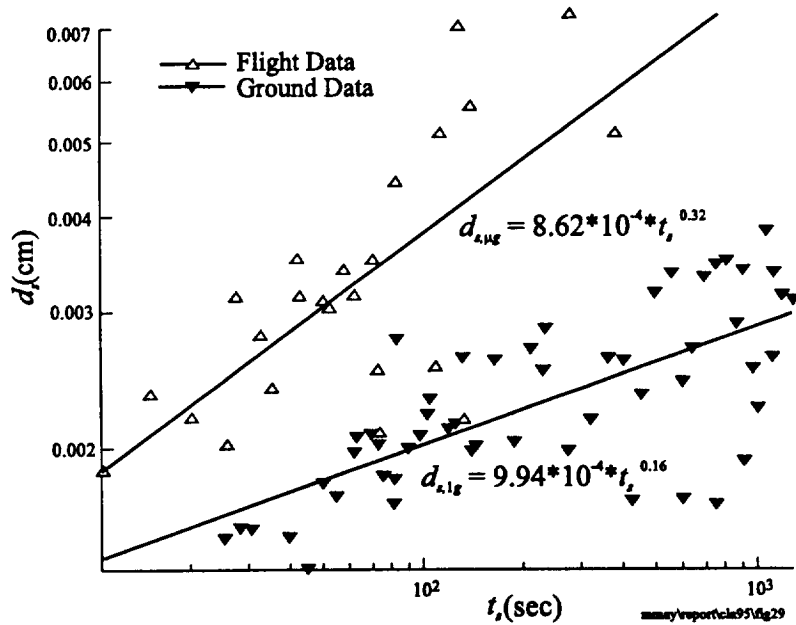


Figure 29. Logarithmic Representation of Secondary Dendrite Arm Spacing as a Function of Local Solidification Time for Microgravity and Ground-Based Dendritic Directional Solidification.

A second representation of the data as seen in Figure 30 provides further information. The cube of secondary arm spacing is plotted as a function of local solidification time. A linear curve fit through the flight and through the ground-based data allows the application of the following relationship proposed by Kirkwood⁴¹ for secondary arm coarsening during solidification

$$d_s^3 = \frac{128\gamma DT}{mC_0(k_p - 1)F}t_s + d_0^3 \quad (3)$$

where d_0 is the initial side branch spacing, D is the solutal diffusivity, γ is the surface energy, T is temperature, m is the slope of the liquidus, C_0 is the solute content of the alloy, k_p is the solute partition coefficient, and F is the heat of fusion. The straight line fit for the flight and ground-based data are:

$$\begin{aligned} d_s^3 \text{ (microgravity)} &= 79 \times 10^{-11}t_s + 3.2 \times 10^{-9} \\ d_s^3 \text{ (ground-based)} &= 2.2 \times 10^{-11}t_s + 7.3 \times 10^{-9}. \end{aligned} \quad (4)$$

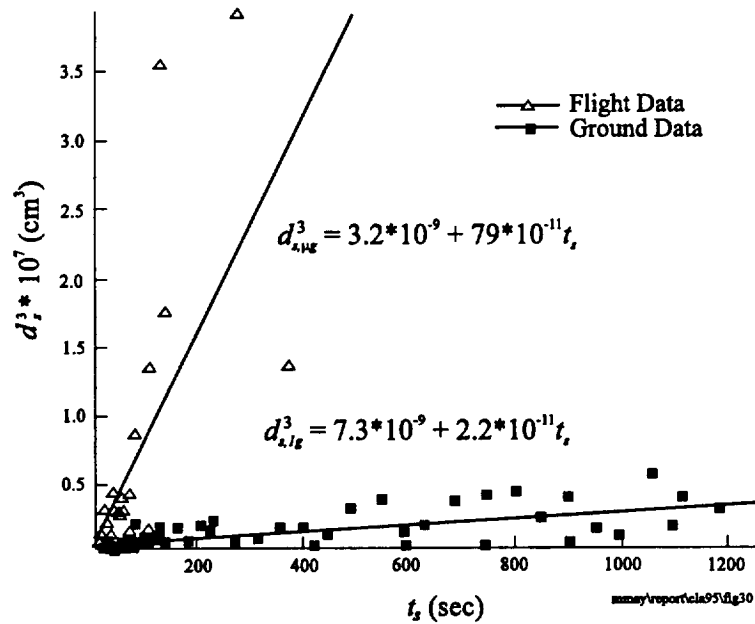


Figure 30. Secondary Dendrite Arm Spacing as a Function of Local Solidification Time for Microgravity and Ground-Based Dendritic Directional Solidification.

Taking the ratio of the microgravity to the ground-based slopes and assuming that all of the parameters except diffusion are unaffected by gravity, the flight diffusivity is found to be 35 times that of the ground. (The calculated diffusivities are 4.7×10^{-4} for the flight experiments and 1.3×10^{-5} for the ground experiments. These are in the acceptable range for diffusivities and the ground value is similar to that in the literature,³⁷ i.e., 2.3×10^{-5} cm²/sec.) This smaller diffusion coefficient on earth is precisely the effect that would be obtained if fluid flow is interfering with the interdendritic diffusion.⁴² Mass transport between coarsening dendrite arms is generally considered to be due to interdendritic diffusion. However, convective fluid motion will interfere with the diffusion couple between arms and will reduce the extent of coarsening and result in smaller arm spacings such as obtained on earth. This is illustrated in Figure 31, which describes the diffusion field and resultant coarsening for dendrites in stagnant and flowing liquid.

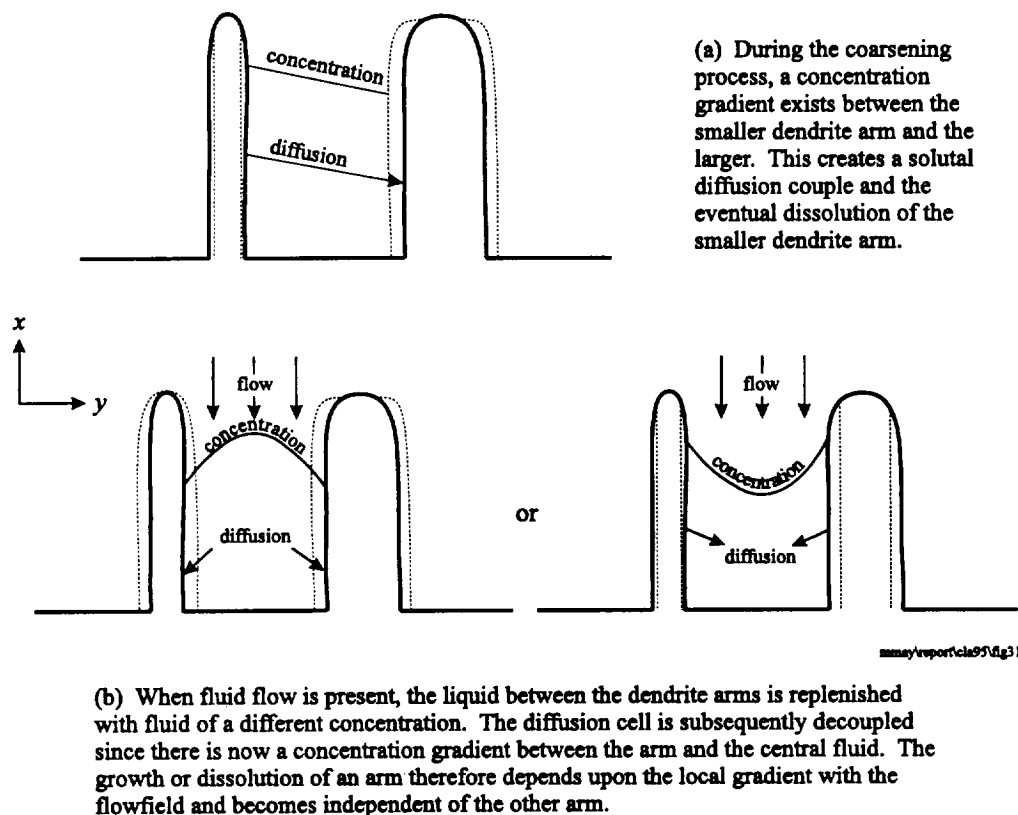


Figure 31. Simplified Description of a Coarsening Mechanism for Dendrite Secondary Arms and the Disruption Caused by Interdendritic Fluid Flow. The concentration field between dendrite arms influences the coarsening process as seen in (a). When fluid flow is present, the coarsening process is altered as shown in (b).

Such a modification to the interdendritic solutal diffusion fields due to convection can be examined simply by approximating the dendrites as infinite flat plates with solutal boundary conditions typical of $\text{NH}_4\text{Cl-H}_2\text{O}$ dendrites. A fully developed convective flow-field of mean velocity U_m flows into the area between dendrites (infinite plates) separated by a distance $2s$. The equations governing this situation are

$$\frac{dP}{dx} = \mu \frac{d^2 u}{dy^2} \quad (5)$$

$$u \frac{\partial C}{\partial x} = D \frac{\partial^2 C}{\partial y^2} \quad (6)$$

with the inlet condition

$$C(0, y) = C_0 \quad (7)$$

and the boundary conditions

$$u(x, s) = u(x, -s) = 0 \quad C(x, -s) = C_1 \quad C(x, s) = C_2. \quad (8)$$

Substituting the following non-dimensional quantities

$$X = \frac{x}{s}, \quad Y = \frac{y}{s}, \quad U = \frac{u}{U_m}$$

$$\Phi = \frac{1}{Pe} \frac{\Omega_i}{\Omega_f} \left(\frac{C_1}{C_1 - C_2} \right)$$

where

$$Pe = \frac{U_m s}{D}, \quad \Omega_i = \left(\frac{C_1 - C_0}{C_1} \right), \quad \Omega_f = \left(\frac{C_1 - C_0}{C_1 - C} \right) \quad (9)$$

Pe is the mass transfer Peclet number, Ω_i is supersaturation at the $y = -s$ dendrite interface, and Ω_f is the field varying supersaturation. The equations become

$$\frac{d^2 U}{dY^2} = E \quad (10)$$

$$Pe U \frac{\partial \Phi}{\partial X} = \frac{\partial^2 \Phi}{\partial Y^2} \quad (11)$$

where the dimensionless pressure gradient is

$$E = \frac{\frac{dP}{dx} s^2}{\mu U_m} \quad (12)$$

The inlet condition is now

$$\Phi(0, Y) = \Phi_0 \quad (13)$$

and the boundary conditions are

$$\Phi(x, -1) = \Phi_1, \quad \Phi(x, 1) = \Phi_2. \quad (14)$$

The velocity profile is the parabolic distribution

$$U(Y) = \frac{E}{2}(Y^2 - 1) \quad (15)$$

and the solute equation becomes

$$Pe \frac{E}{2}(Y^2 - 1) \frac{\partial \Phi}{\partial X} = \frac{\partial^2 \Phi}{\partial Y^2}. \quad (16)$$

This equation was solved numerically using a Crank–Nicholson (CN) x -marching technique.

A half-spacing dimension of 50 μm was selected for examination based on experimental observation. The solutal boundary conditions were determined by assuming a fixed dendrite radius $r_2 = 50 \mu\text{m}$ for one wall and varying the radius of the other dendrite, $.1 \mu\text{m} < r < 1000 \mu\text{m}$. The capillary modification to the equilibrium concentration is a function of the surface energy, the molar volume, and the local temperature as

$$C_{\text{eq}}^* = C^* \left(1 - \left(\frac{2\gamma V^\beta}{RT} \right)^\alpha H \right) \quad (17)$$

where H is the curvature of the interface ($1/r$). The values in Table 4 were used for this study.

TABLE 4 Parameters used in Calculation

$r_2 = 50 \mu\text{m}$	$\gamma = 40 \text{ ergs/cm}^2$
$r = 0.1 - 1000 \mu\text{m}$	$R = 8.314 \text{ J/mol K}$
$V^\beta = 35 \text{ cm}^3/\text{mol}$	$C' = 72.63 \text{ wt\% H}_2\text{O}$
$T = 293 \text{ K}$	$D = 2.3e-5 \text{ cm}^2/\text{sec}$
$\mu = .01 \text{ g/cm sec}$	$U_m = .01 \text{ cm/sec}$
$dP/dx = -1000 \text{ g/cm}^2 \text{ sec}^2$	$C_2 = 76.62832951 \text{ wt\% H}_2\text{O}$

The values for dP/dx and U_m were estimated from both experimental observations^[13] and calculations using the Fluids Thermal Model,^[25] a non-linear model of solidification

with convection. Thus, for selected values of r with its associated equilibrium concentration, the solute concentration at the inlet was varied to determine its influence on the solute profiles between the approximated dendrites. In particular, the dependence of the wall solute gradients on the inlet concentration was desired, since this will dictate whether the dendrite is growing or melting.

The inlet concentration has a strong influence on the solutal profiles between the dendrites and the resultant concentration gradients at the walls. This is of particular interest because these gradients determine whether or not the solution is favorable for growth. Using the criteria that a positive dC/dy promotes melting and a negative dC/dy promotes growth, the growing and melting regimes for a dendrite arm can be determined. In this case a negative gradient is diffusing water away from the wall (favorable for growth), and a positive gradient is diffusing water into the wall (favorable for melting). Figure 32 shows the conditions which distinguish the regimes for various arm radii and inlet concentrations at a selected flow rate and secondary arm spacing. As expected, the larger the radius, the greater the propensity for growth. The plot illustrates that a single dendrite arm can melt or grow depending upon its radius and the flow solutal conditions. When arms with different radii exist adjacent to each other it is also possible that one could be growing while the other is melting. Therefore, three regimes exist for the pair of dendrite arms: 1) both growing, 2) large growing; small melting (generally termed coarsening), and 3) both melting.

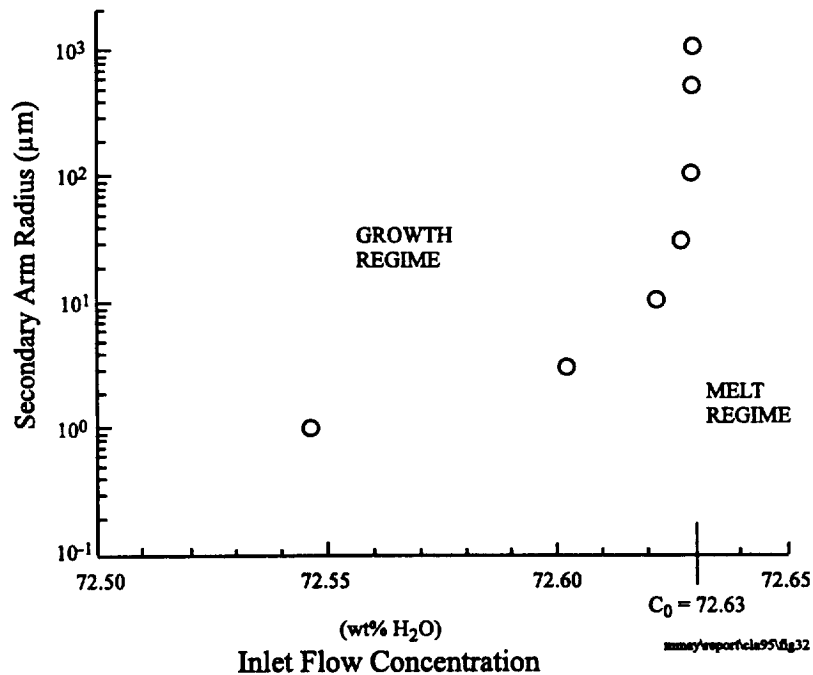


Figure 32. Identification of the Growth and Melt Regimes for Secondary Dendrite Arms as Determined by the Secondary Arm Radius and the Inlet Flow Concentration for the Conditions in Table 4.

The sensitivity of each dendrite arm's diffusion layer gradients to the inlet concentration suggests that convective effects can be important even at low levels of convective motion. This is significant for coarsening studies performed on the ground, for which some level of convective motion is almost assured. The necessity for a baseline case, such as accomplished in microgravity, is therefore evident.

Computational Model Results

The physical properties of the $\text{NH}_4\text{Cl-H}_2\text{O}$ and quartz, the experiment top and bottom temperature, the cooling rate and the gravitational level were the primary inputs for the experiment specific model. Concentration, temperature, fraction of liquid, kinetic energy, streamlines, and flow velocity vectors were calculated for the same applied temperature gradient and cooling rate at 10^0g_e , $10^{-1}g_e$, $10^{-2}g_e$, $10^{-3}g_e$, $10^{-4}g_e$, and $10^{-5}g_e$.⁴³

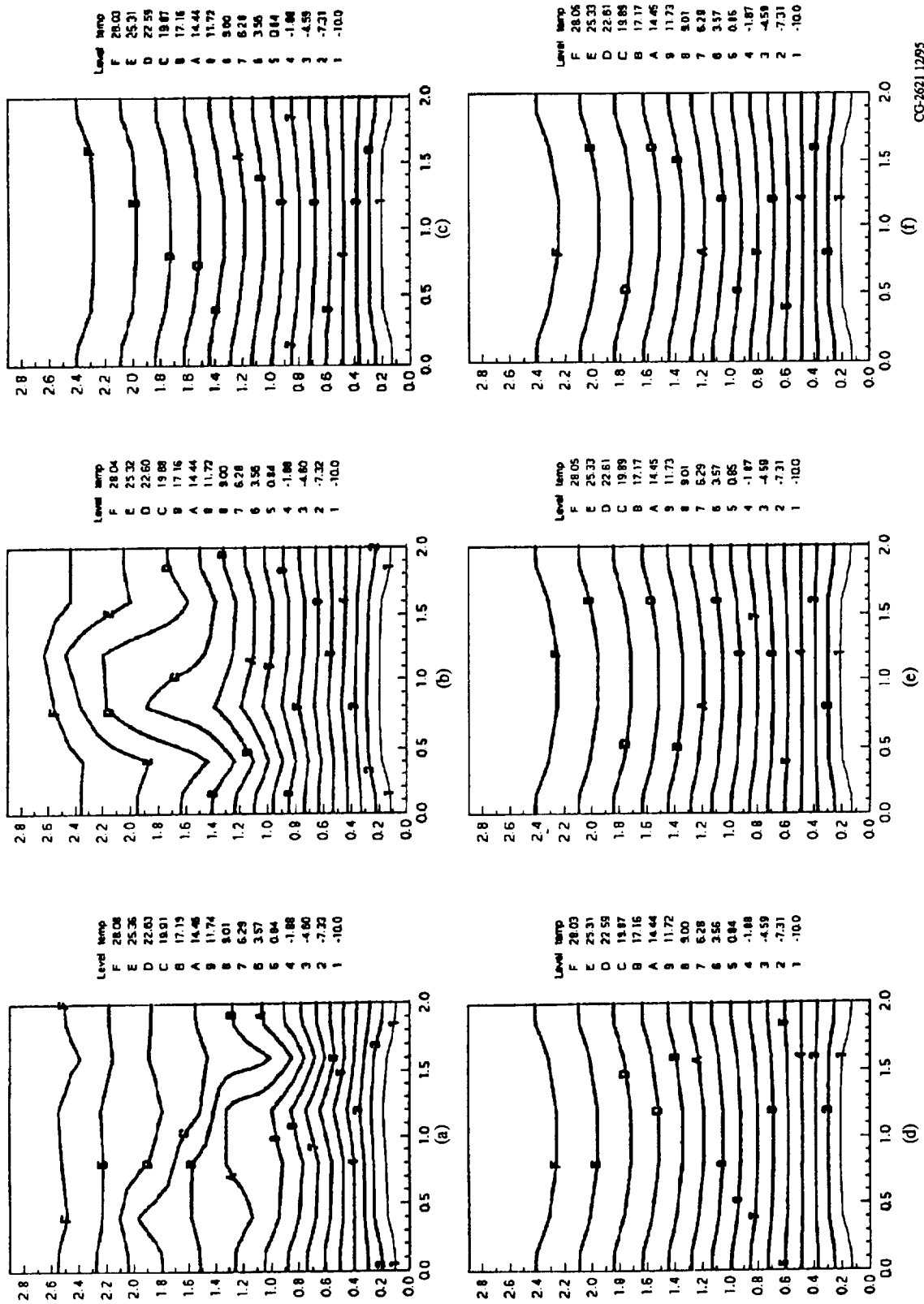
The 10^0g_e and $10^{-5}g_e$ growth rates were measured in the ground based and International Microgravity Laboratory I experiments for the final twenty minutes of solidification. These are given in Table 5 along with the computationally predicted growth rates (fitted linear slopes).

TABLE 5

Condition	Growth Rate (cm/hr)
10^0g_e measured	1.59
10^0g_e predicted	1.52
$10^{-5}g_e$ measured	3.30
$10^{-5}g_e$ predicted	3.36

The computational model predictions are very similar to the measured values, indicating that the model is an accurate representation of $\text{NH}_4\text{Cl-H}_2\text{O}$ dendritic growth. Other significant comparisons such as development of the inverted density layer and time of convective onset were also closely matched.

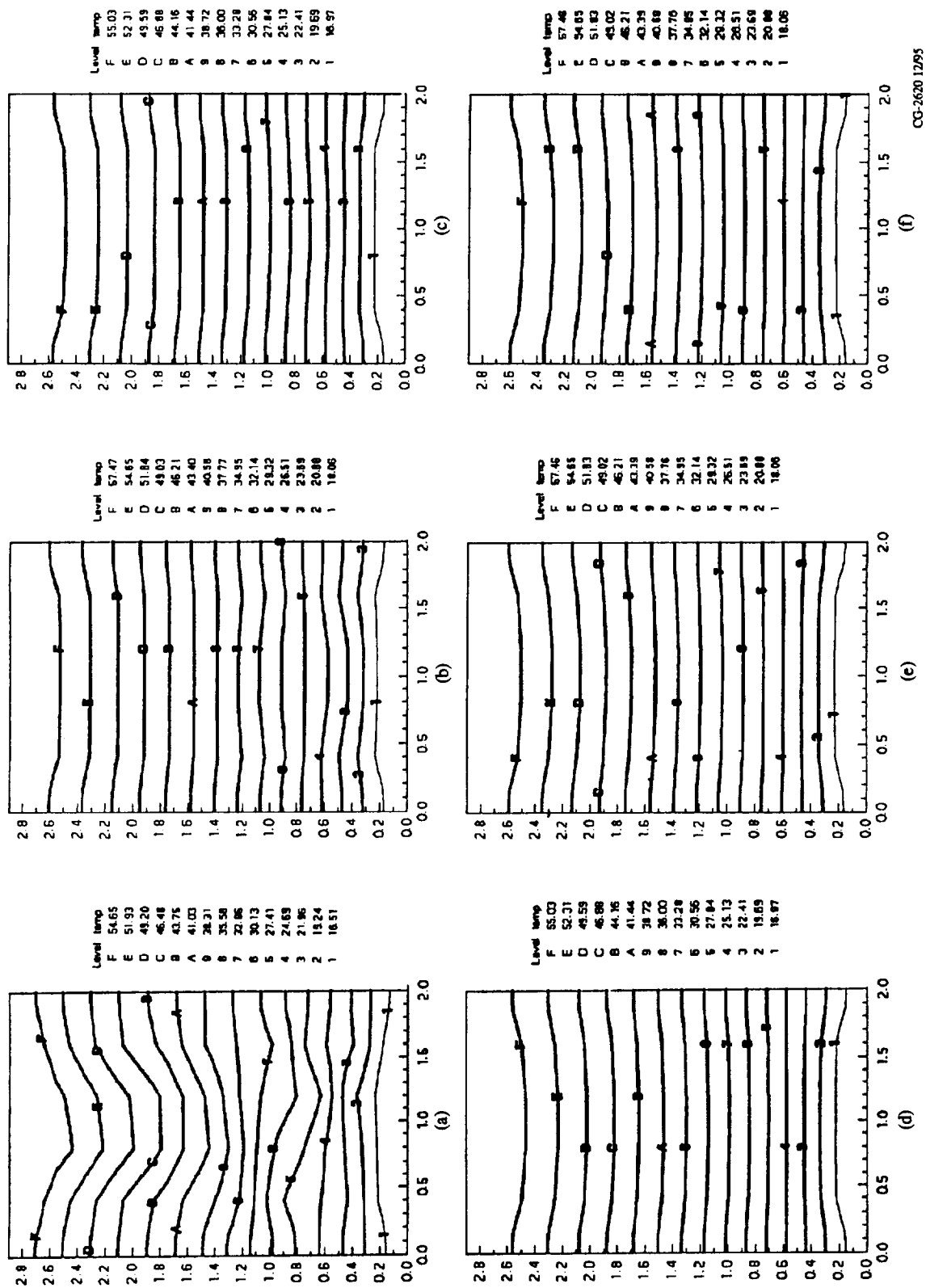
Applying the model to each order of magnitude gravity level from 10^0g_e to $10^{-5}g_e$, the isotherms, isoconcentrates, streamlines, kinetic energy and mushy zone heights were calculated. The isotherms, isoconcentrates and streamlines are given in Figures 33 through 38 at 360 seconds and 1800 seconds after initiation of growth for the six gravity levels. Figure 39 shows the predicted mushy zone heights as a function of time. During the early time period, the highest gravity level (10^0g_e) has the greatest initial growth. This can be more easily seen in the expanded view in Figure 40 which also shows that $10^{-1}g_e$ and $10^{-2}g_e$ demonstrate a similar increase though at later times. This early time period increase is caused by the onset of convection which makes fresh solute available to the dendritic front, thereby enhancing the growth. This effect is minimal at $10^{-3}g_e$ and absent at the higher gravity levels.



CG-2621.12/95

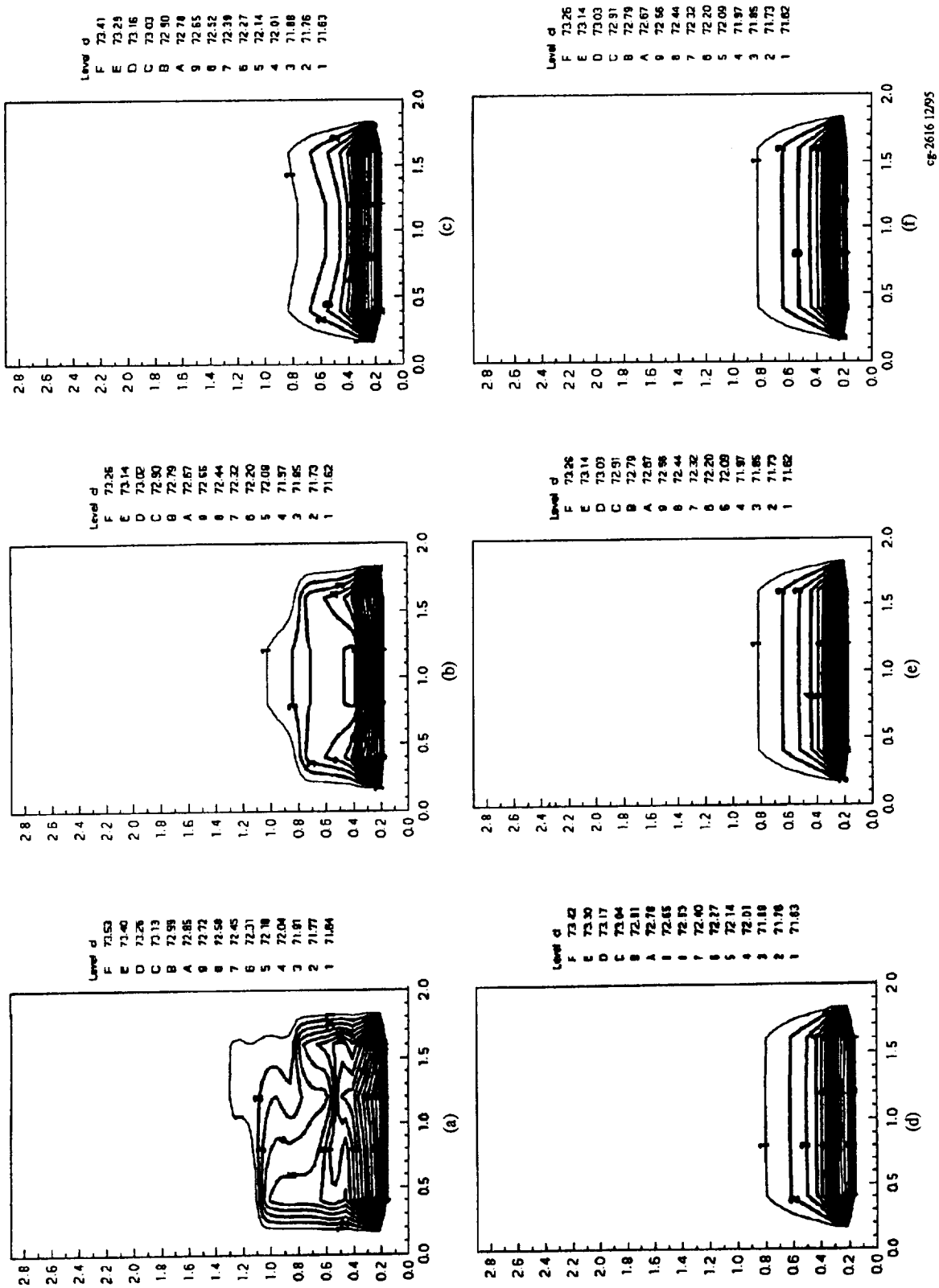
Predicted isotherms for 1800 seconds for (a) $10^0 g_e$, (b) $10^{-1} g_e$, (c) $10^{-2} g_e$, (d) $10^{-3} g_e$, (e) $10^{-4} g_e$, (f) $10^{-5} g_e$.

Figure 33.



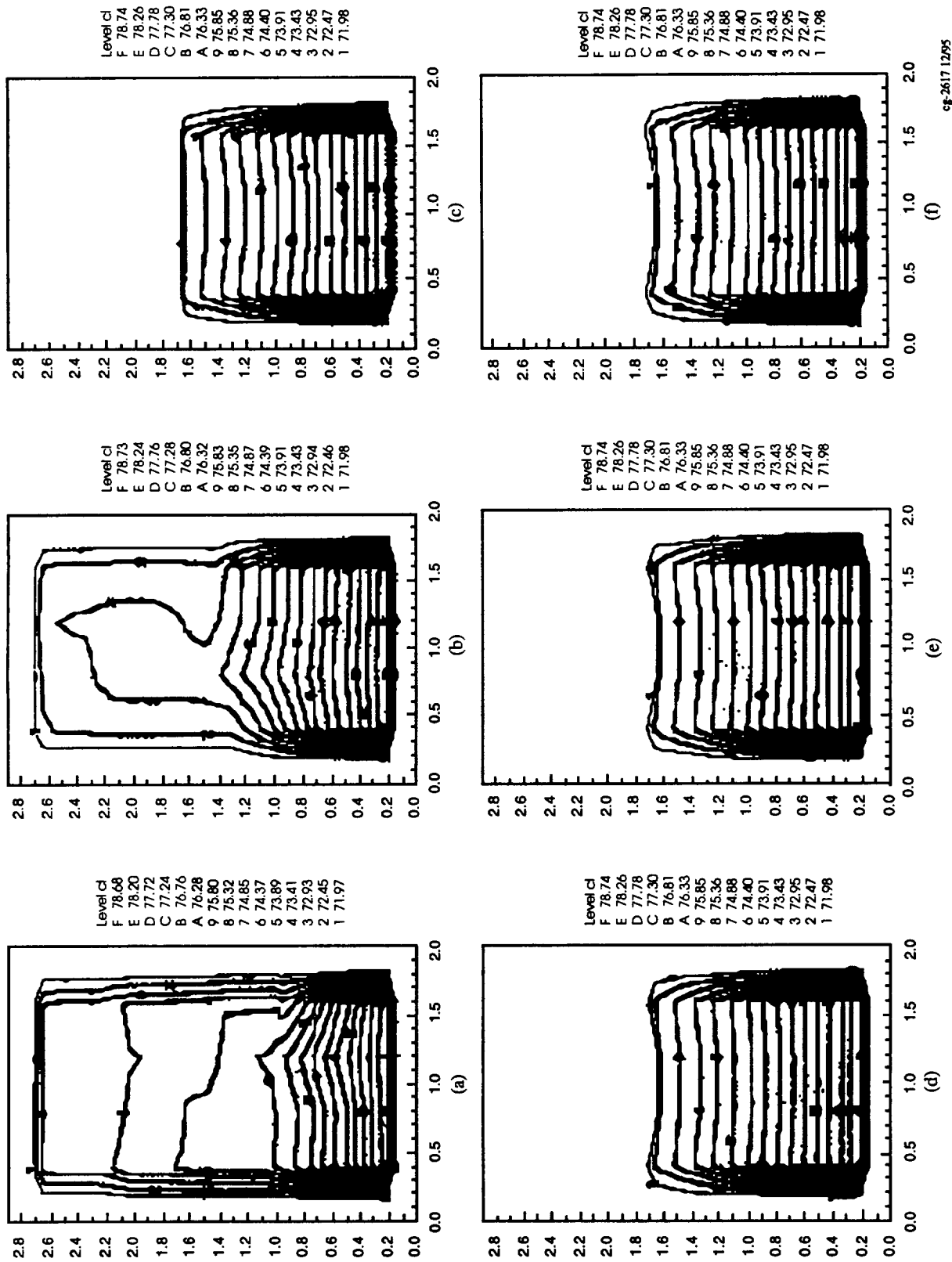
Predicted isotherms for 360 seconds for (a) $10^0 g_e$, (b) $10^1 g_e$, (c) $10^2 g_e$, (d) $10^3 g_e$, (e) $10^4 g_e$, (f) $10^5 g_e$.

Figure 34.



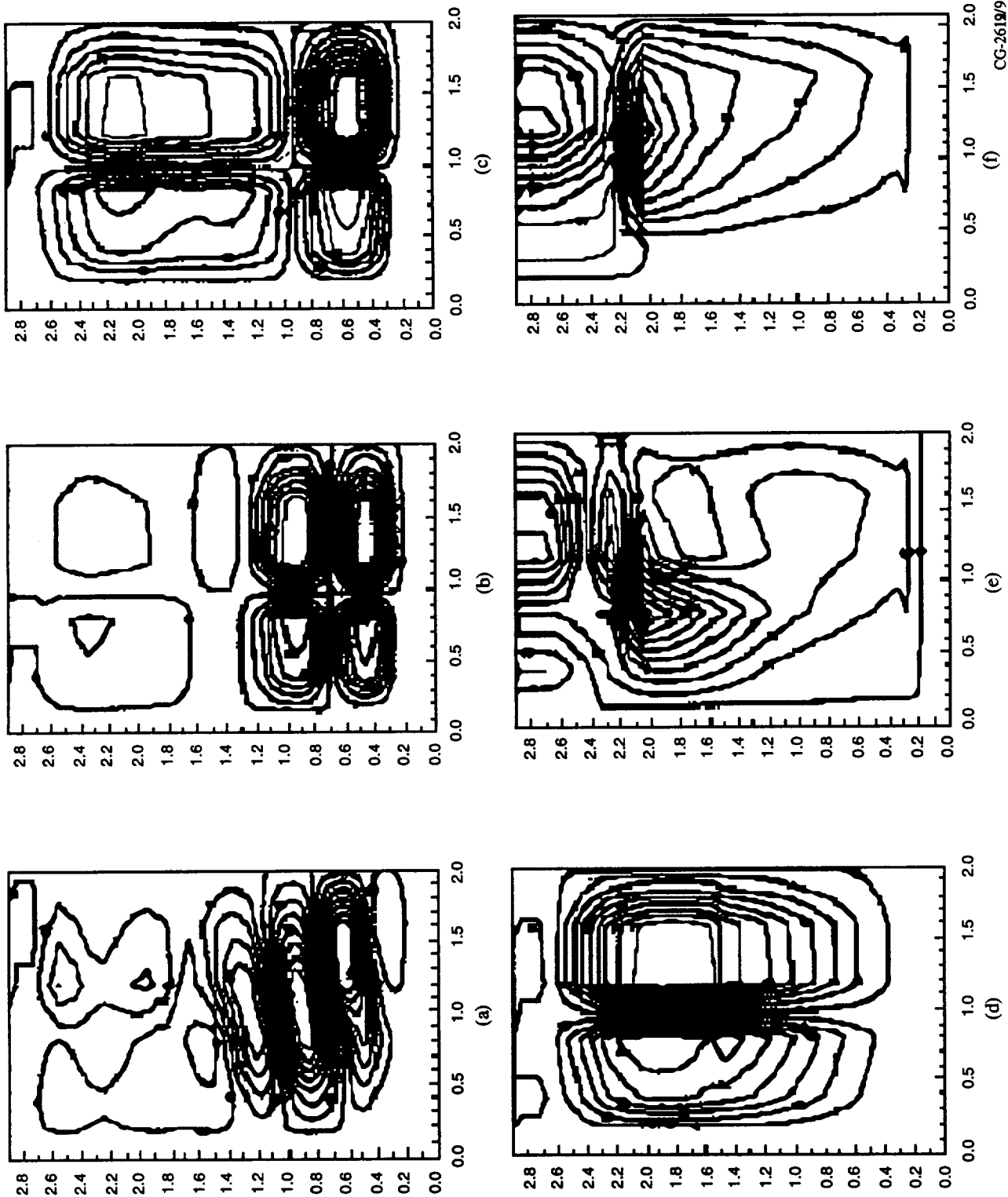
Predicted isotherms for 360 seconds for (a) $10^0 g_e$, (b) $10^{-1} g_e$, (c) $10^{-2} g_e$, (d) $10^{-3} g_e$, (e) $10^{-4} g_e$, (f) $10^{-5} g_e$.

Figure 35.



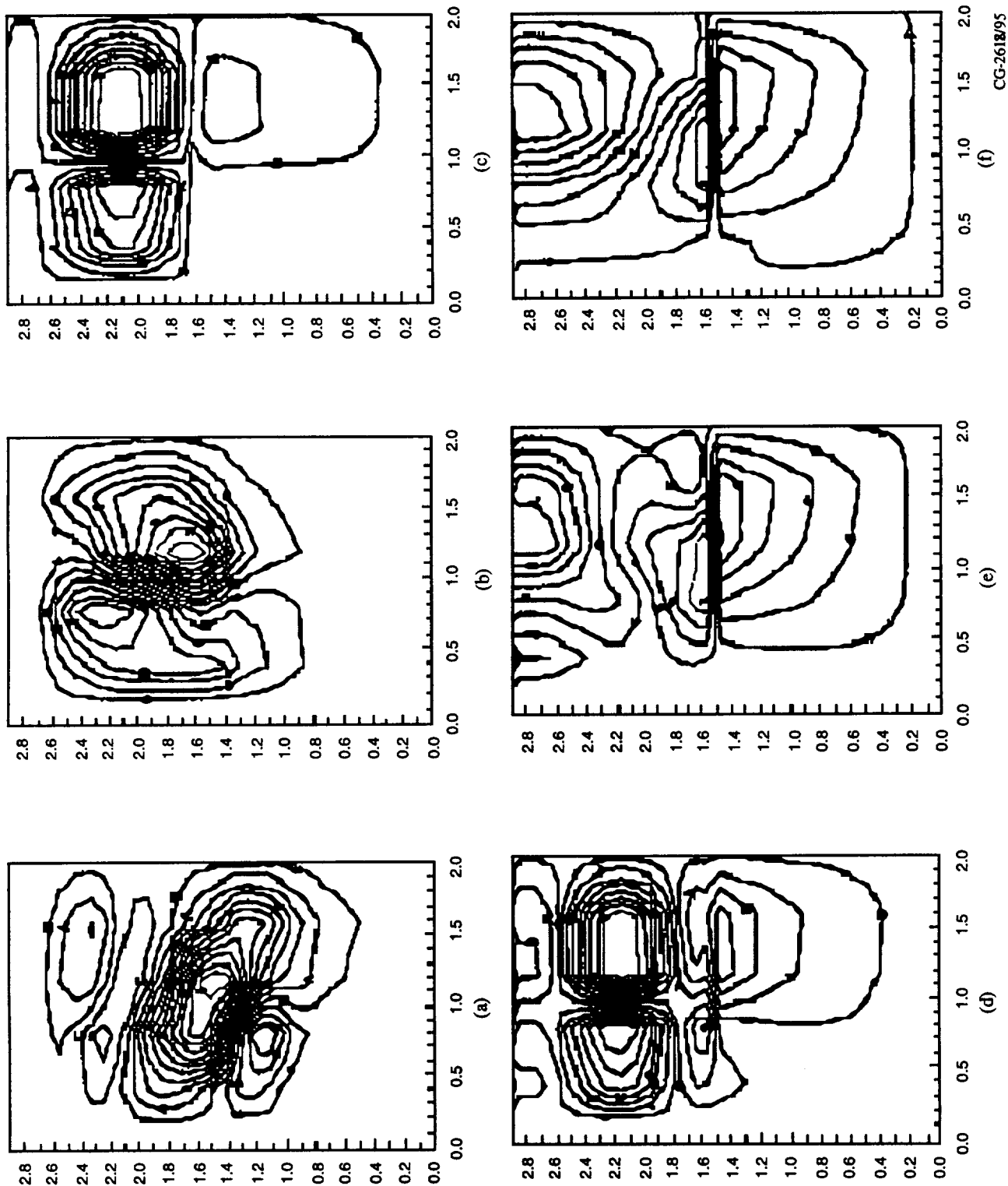
Predicted isoconcentrates at 1800 seconds for (a) 10^0g_e , (b) 10^{-1}g_e , (c) 10^{-2}g_e , (d) 10^{-3}g_e , (e) 10^{-4}g_e , (f) 10^{-5}g_e .

Figure 36.



Predicted streamlines at 360 seconds for (a) $10^0 g_e$, (b) $10^{-1} g_e$, (c) $10^{-2} g_e$, (d) $10^{-3} g_e$, (e) $10^{-4} g_e$, (f) $10^{-5} g_e$.

Figure 37.



Predicted streamlines at 360 seconds for (a) $10^0 g_e$, (b) $10^{-1} g_e$, (c) $10^{-2} g_e$, (d) $10^{-3} g_e$, (e) $10^{-4} g_e$, (f) $10^{-5} g_e$.

Figure 38.

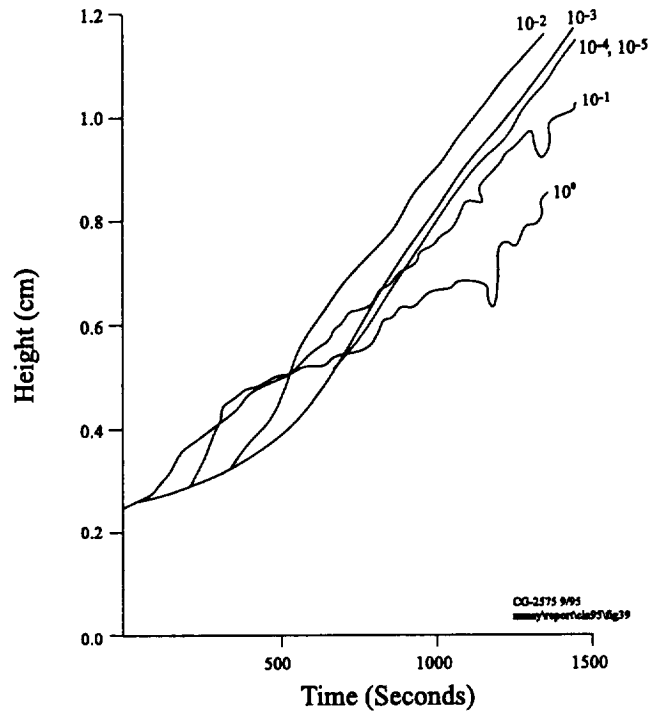


Figure 39. Predicted mushy zone height as a function of time for six gravity levels from $10^0 g_e$ (earth) to $10^{-5} g_e$.

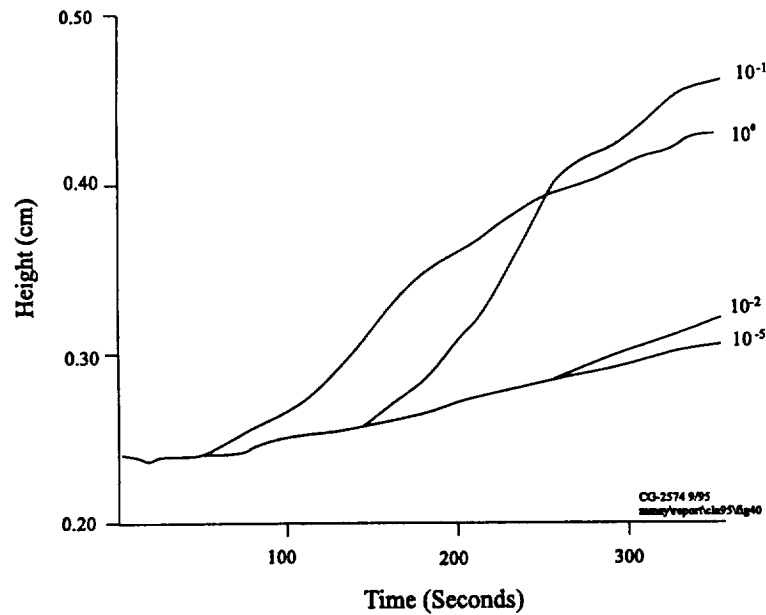


Figure 40. Expanded view of predicted mushy zone height as a function of time for $10^0 g_e$, $10^{-1} g_e$, $10^{-2} g_e$, and $10^{-5} g_e$.

Once steady growth is achieved, the highest gravity level has the lowest growth rate, with the growth rate increasing with decreasing gravity level until $10^{-4}g_e$ is reached. The growth rates of $10^{-4}g_e$ and $10^{-5}g_e$ are equivalent. Again, convection (or its absence) is the dominating influence in this effect. The flow which occurred at the higher g-levels altered the concentration of the bulk liquid into which the dendritic front is growing. The results of this can be seen in Figure 41 which shows the centerline concentration as a function of height for 10^0g_e , $10^{-1}g_e$ and $10^{-5}g_e$ at 1800 seconds. The location of each interface is noted on the plot. Due to the convective mixing, the 10^0g_e interface is growing into more dilute solution than the lower gravity level interfaces. The $10^{-5}g_e$ interface grows into the most concentrated solution and hence at the same cooling rate and applied temperature gradient, grows the fastest. It is these later time period growth rates which were compared with experiment.

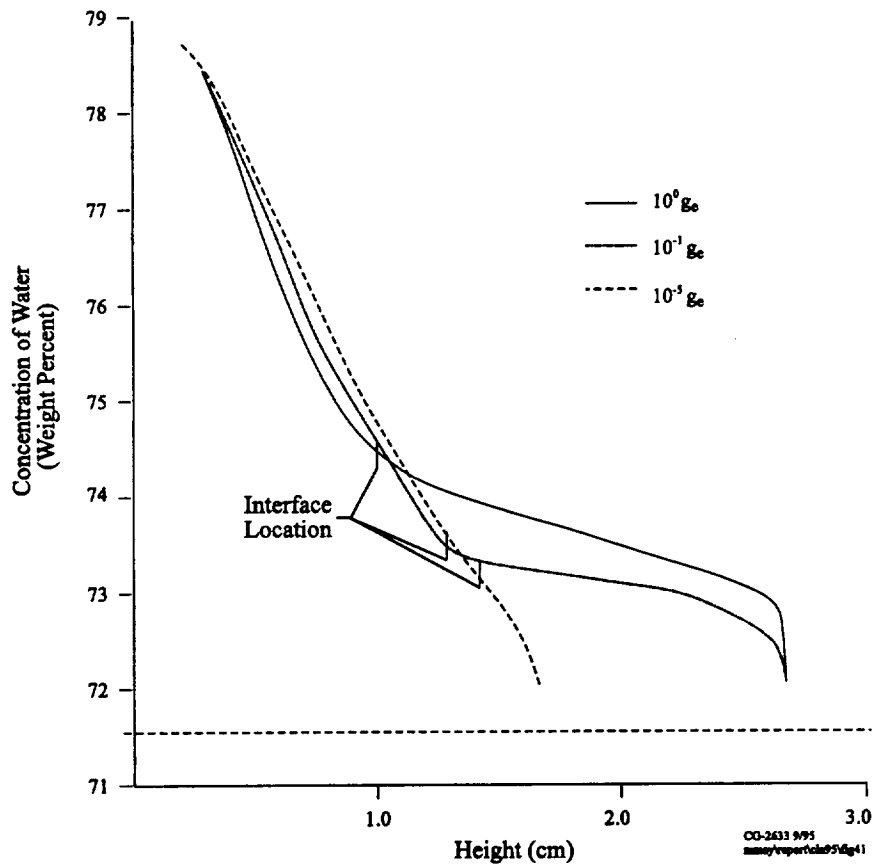


Figure 41. Centerline concentration of H₂O in the liquid as a function of cuvette height. The interface location is noted by the vertical line.

The model predictions show that the fluid flow and hence gravitational level has the greatest impact (as expected) at the higher gravity values. As the gravitational levels decrease, so do the maximum flow velocities as can be seen in Figure 42. The effect with gravity is linear. However, at $10^{-3}g_e$ and lower, the flow velocities approach the same values, those of zero-gravity (an additional case computed for baselining the results). Figure 43 shows the streamlines for the zero-gravity prediction. The flow is centered around the shrinkage tube and does not appear to significantly penetrate the mushy zone.

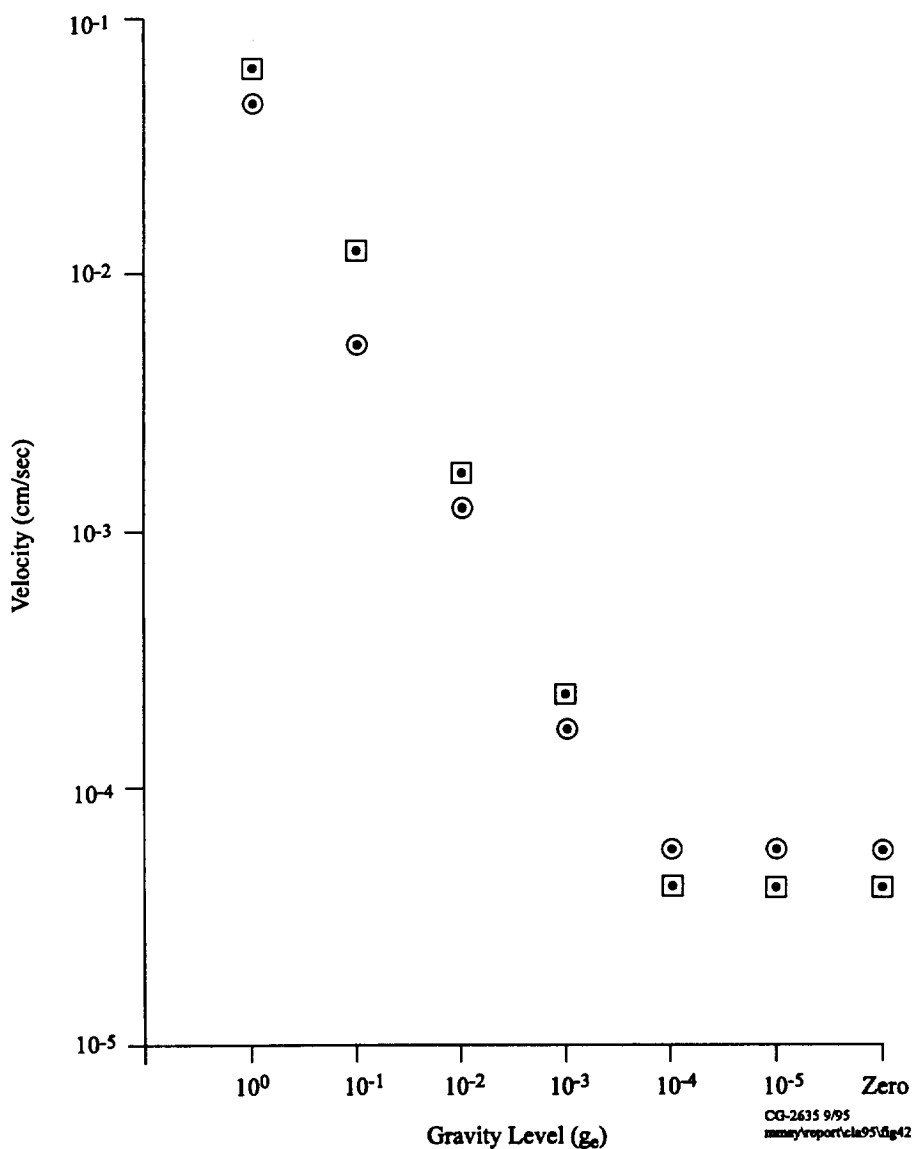


Figure 42. Predicted maximum fluid flow velocity as a function of gravity level.

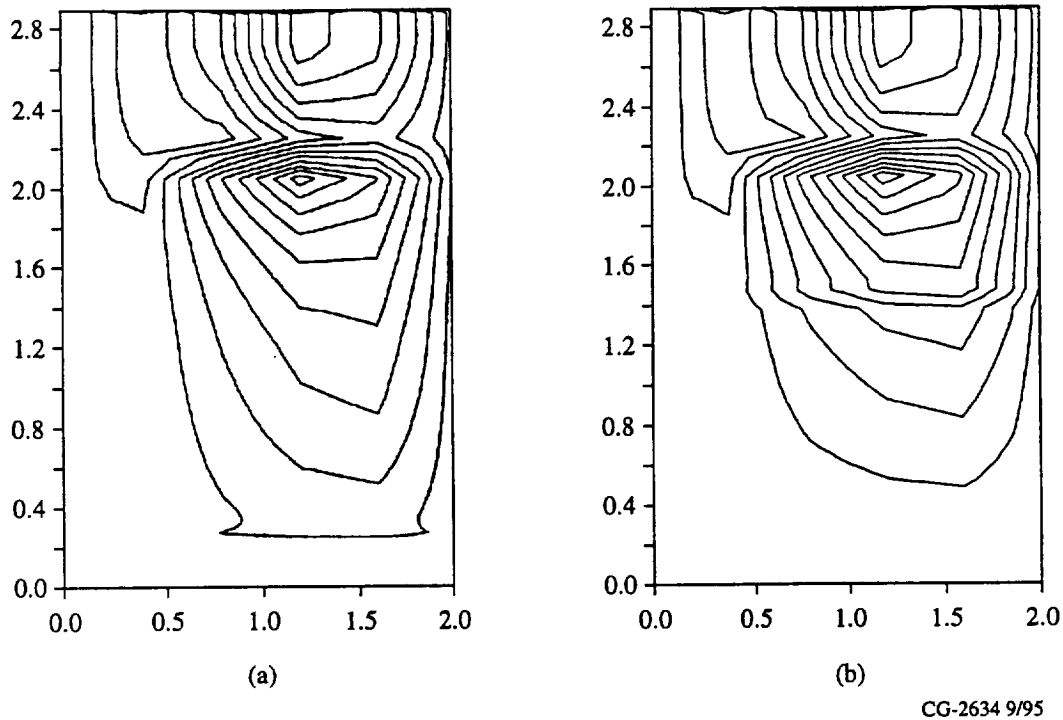


Figure 43. Predicted zero-gravity streamlines at (a) 360 s and (b) 1800 s.

The kinetic energy predictions are shown in Figure 44. Since the maximum flow velocities, the concentration fields and therefore the growth rates do not significantly change below $10^{-4}g_e$, it can be concluded that energies in the 10^{-8} erg range and lower produce no significant effect on the dendritic growth. Therefore, gravity levels and/or other experiment parameters which allow the kinetic energy of the system to remain below this range would produce acceptable low-gravity dendritic solidification.

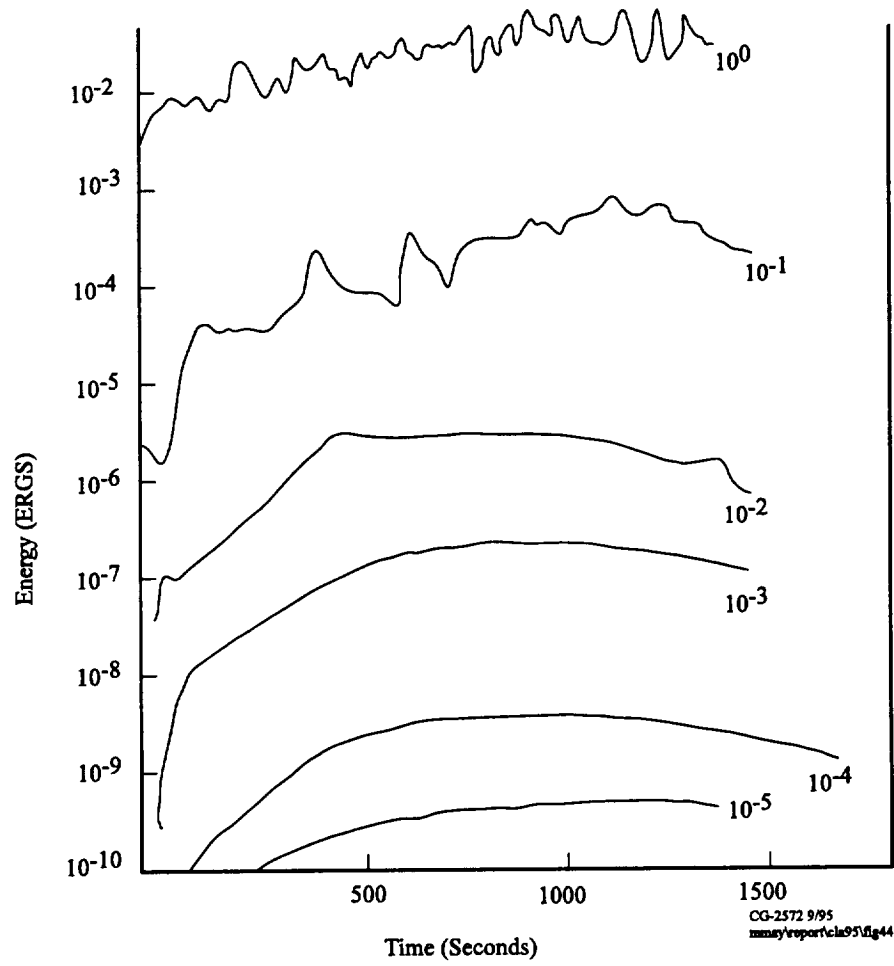


Figure 44. Predicted kinetic energy as a function of time for six gravity levels from $10^0 g_e$ (earth) to $10^{-5} g_e$.

VI. Conclusions

Measured ground-based dendritic growth front rates in the $\text{NH}_4\text{Cl-H}_2\text{O}$ system were approximately one-half that of microgravity growth rates for identically applied solidification conditions. In addition, the density of the mushy zone was significantly increased by processing on earth. Both of these results are due to the presence of bulk convection and its influence on fluid concentration. Although thermal transport is also affected, temperature measurements indicated the result to be minimal compared to the concentration. When convection occurs during the growth process, the overall length of the dendrites (and therefore their growth rate) is reduced by the increasing depletion of the bulk liquid due to mixing with the interdendritic liquid. In contrast, the dendrite stalks within the mushy zone are subjected to fluid with enhanced concentration of solute and therefore thicken and coarsen, producing a denser structure and smaller secondary arm spacings. The magnitude of this effect is strongly dependent upon the relative sizes of the mushy zone and the bulk liquid regions and also, of course, the gravitational level. Computational model results suggest that gravity levels which allow the kinetic energy range to remain below 10^{-8} ergs provide acceptable low gravity solidification.

A comparison of diffusion layer widths ahead of $\text{NH}_4\text{Cl-71.5 wt\% H}_2\text{O}$ dendritic growth fronts during microgravity ($10^{-5} g_e$) and ground-based experiments indicates that while the flight experiments follow the expected $2D/V$ relationships, the ground-based experiments exhibit the effects of both micro and macroconvection. Dendrite stalk boundary layer flows are suspected based upon the data, often enlarging the layer beyond that commensurate with theory, but cellular convective breakdown ultimately limits the maximum size of the layer to a value commensurate with a critical Rayleigh number. The evidence of the static boundary layer flows creates serious concerns for achieving true diffusion-limited growth on earth.

VII. PI Team

The individuals participating in this program represent an accumulation of expertise in the areas of analytical modeling, solidification, Fourier optics and microgravity processing. The Principal Investigator team consists of UTSI faculty and staff members Dr. Mary Helen McCay, Dr. T. Dwayne McCay, Dr. L. Montgomery Smith and Dr. John Hopkins. CAST team members who have participated in the program and left UTSI after graduation are Dr. Sam Lowry, Ms. Mary Magnani (M.S. degree), Perry Gray (M.S. degree), and Ram Sivarakumaran (M.S. degree). Dr. Robert Owen participates as a team member from the University of Colorado, Mr. Ron Porter and Mr. Arthur Henderson are team members at MSFC. Dr. Martin E. Glicksman from Rensselaer Polytechnic Institute participates as a USRA consultant.

Principal Investigator - Dr. Mary Helen McCay is the Principal Investigator on the CAST I experiment. She has been involved with flight experiments since Skylab and has been the PI on NASA SPAR experiments involving both metal-models and alloy systems. Dr. McCay is responsible for the overall direction of the experiment.

Co-Principal Investigator - Dr. T. Dwayne McCay is the Co-Principal Investigator on the CAST I experiment and has been responsible for developing the non-linear analytical solidification model. The model predicts diffusion dominated solidification, the onset of convective instabilities and the fluid flow field that occurs during directional growth of dendritic systems.

Co-Investigator - Dr. L. Montgomery Smith is responsible for developing the optical and digital image processing techniques for analysis of the diffusion layer and flow fields.

Co-Investigator - Dr. John A. Hopkins is a significant participant in the CAST I experiment. He developed an interferometric technique for determining concentration profiles within the diffusion layer for his Master's thesis and built a computational linear stability model as part of his PhD dissertation.

The work is being conducted in the Center for Laser Applications (CLA) at The University of Tennessee Space Institute (UTSI). UTSI is a graduate education and research institute of the University of Tennessee, Knoxville. Established near the U.S. Air Force Arnold Engineering Development Center, UTSI has evolved into an internationally recognized institution for study and research in engineering, physics, mathematics and computer sciences.

The Center for Laser Applications contains both the facilities and the individuals required to successfully accomplish the CAST experiment program. Their major equipment includes numerous lasers, optical digital analyzers, metal model solidification and optical visualization apparatus, microscopes (metallograph, SEM and microprobe), standard metallography equipment, and computer systems.

Both pre- and post-flight data analysis were performed in large part on the digital image processors located in the CLA laboratory. As mentioned previously, a spatial phase Fourier transform technique has been developed by the authors to analyze the CAST holograms.

VIII. References

1. J. W. Rutter and B. Chalmers, *Can. J. Physics* 31, 15 (1953).
2. W. W. Mullins and R. F. Sekerka, *J. Appl. Phys.* 35, 444 (1964).
3. S. R. Coriell, M. R. Cordes, W. J. Boettinger and R. Sekerka, *Journal of Crystal Growth*, 49, 13-28 (1980).
4. J. J. Favier and A. Rouzaud, *J. Crystal Growth* 74, 367 (1983).
5. M. C. Flemings and G. E. Nereo, *Trans. A.I.M.E.* 239, 1449 (1967).
6. M. C. Flemings, R. Mehrabian and B. E. Nereo, *Trans. A.I.M.E.* 242, 41 (1968).
7. M. C. Flemings and G. E. Nereo, *Trans. A.I.M.E.* 242, 50, (1968).
8. R. Mehrabian, M. Keane and M. C. Flemings, *Met. Trans.* 1, 1209 (1970).
9. S. Kou, D. Poirier and M. C. Flemings, *Met. Trans.* 9B, 711, (1978).
10. I. Fujii, D. R. Poirier and M. C. Flemings, *Met. Trans.* 10B, 331 (1979).
11. R. J. Naumann and H. W. Herring, NASA SP-443, National Aeronautics and Space Administration, Washington D.C. (1980).
12. A. C. Fowler, *J. of Applied Mathematics* 35, 159 (1985).
13. M. H. McCay and T. D. McCay, *J. of Crystal Growth* 126, 223-228 (1993).
14. M. H. McCay and T. D. McCay, *J. Thermophysics and Heat Transfer* 2, 197 (1988).
15. P. Gray, Masters Thesis, University of Tennessee, Knoxville, May 1989.
16. T. D. McCay, M. H. McCay and P. A. Gray, *Phys. Rev. Letters*, 2060-2063 (1989).
17. J. W. Goodman, *Introduction to Fourier Optics*, (McGraw-Hill, San Francisco, 193 (1968).
18. M. Born and E. Wolf, *Principles of Optics*, Sixth Ed., (Pergamon Press, Oxford, 193 (1980).
19. M. H. McCay, T. D. McCay and L. M. Smith, *Applied Optics*, 29, 5, 699-703 (1990).
20. M. E. Magnani, Masters Thesis, University of Tennessee, Knoxville, December 1991.
21. J. A. Hopkins, T. D. McCay and M. H. McCay, AIAA paper 91-1334, AIAA 26th Thermophysics Conference, Honolulu Hawaii (1991).
22. M. Takeda, H. Ina and S. Kobayashi, *Journal of the Optical Society of America* 72, 156-160 (1982).
23. R. Sivakumaram, Masters Thesis, The University of Tennessee, December 1994.
24. M. P. Wernet, NASA TM-103270 (1990).
25. S. A. Lowry, Ph.D. Dissertation University of Tennessee, May 1991.
26. S. A. Lowry, T. D. McCay and M. H. McCay, to be submitted to *Metallurgical Transactions*.
27. S. V. Patankar, *Numerical Heat Transfer and Fluid Flow*, Hemisphere Publishing Company (1980).
28. W. D. Bennon, and F. P. Incropera, *Int. J. Heat Mass Transfer*, 30, 10, 2161 (1987).
29. P. J. Prescott and F. P. Incropera, DOE/ER/13759-4 (1991).

30. T. D. McCay, M. H. McCay and J. A. Hopkins, AIAA Paper number 91-1333, AIAA 26th Thermophysics Conference, Honolulu Hawaii (1991).
31. T. D. McCay, M. H. McCay, S. A. Lowry and L. M. Smith, Journal of Thermophysics and Heat Transfer 3, 345 (1989).
32. S. Chandrasekhar, Hydrodynamic and Hydromagnetic Stability, Oxford University Press, 39 (1961).
33. P. Nandapurkar, D. R. Poirier, J. C. Heinrich and S. Felicelli, Met. Trans. B 20B, 711, (1989).
34. M. E. Glicksman, Crystal Properties and Preparation, 22-25 part 1, 11 (1989).
35. S. K. Chan, H. H. Reimer and M. Kahlweit, Journal of Crystal Growth 32, 303 (1976).
36. M. H. Johnston (McCay) and C. S. Griner, Met. Trans. B, 18, 611 (1987).
37. P. G. Grodzka: LMSC-HREC TR D306350, January 1973.
38. M. H. McCay, J. A. Hopkins and T. D. McCay, Metallurgical Transactions, 26A, 227 (1995).
39. M. H. McCay and T. D. McCay, Journal of Crystal Growth, 135, 594 (1994).
40. M. H. McCay, T. D. McCay, and J. A. Hopkins, Journal of Applied Optics, 144, 346 (1994).
41. D. K. Kirkwood, Materials Science and Engineering, 73, L1 (1985).
42. J. A. Hopkins, M. H. McCay, and T. D. McCay, accepted for publication Metallurgical Transactions (1995).
43. T. D. McCay and M. H. McCay, Microgravity Science and Technology, VI/1, 2 (1993).

Appendix: Nomenclature

A_0, B_0	constants
a	wavenumber ($\frac{1}{\text{cm}}$)
B_x	body force in the x direction
C	composition (wt%)
C_e	composition at the eutectic point (wt%)
C_l	solute concentration in the liquid (wt%)
C_l^*	solute concentration in the liquid at the solid-liquid interface (wt%)
C_0	reference composition (wt%)
C_p	specific heat ($\frac{\text{erg}}{\text{gm} \cdot ^\circ\text{C}}$)
C_s	solute concentration in the solid (wt%)
C_s^*	solute concentration in the solid at the solid-liquid interface (wt%)
C_t	solute concentration at the dendrite tip
CR	cooling rate ($\frac{^\circ\text{C}}{\text{time}}$)
d_0	initial side branch spacing (cm)
d_s	secondary arm spacing (cm)
D	solutal diffusion coefficient ($\frac{\text{cm}^2}{\text{sec}}$)
f	spatial frequency ($\frac{1}{\text{cm}}$)
F	heat of fusion
g_e	Earth's gravity ($\frac{980\text{cm}}{\text{sec}^2}$)
g_l	volume fraction of liquid
g_s	volume fraction of solid
G	temperature gradient ($\frac{^\circ\text{C}}{\text{cm}}$)
h	enthalpy ($\frac{\text{ergs}}{\text{gm}}$)
H	interface curvature ($\frac{1}{\text{cm}}$)
H_m	height of the inverted density layer (cm)
H_z	initial height of the mushy zone (cm)
$I(x, y)$	intensity of the light field
ITR	isotherm translation rate ($\frac{\text{cm}}{\text{hour}}$)
J	net flux (e.g., of energy or solute)
k	thermal conductivity ($\frac{\text{erg}}{\text{cm} \cdot \text{sec} \cdot ^\circ\text{C}}$)
k_p	partition coefficient
k_q	thermal conductivity of quartz ($\frac{\text{erg}}{\text{cm} \cdot \text{sec} \cdot ^\circ\text{C}}$)
K	permeability (cm^2)
L	latent heat ($\frac{\text{erg}}{\text{gm}}$)
m	liquidus slope ($\frac{^\circ\text{C}}{\text{wt}\%}$)

P	pressure $\left(\frac{\text{dyne}}{\text{cm}^2}\right)$
Pe	mass transfer Peclet number
P_m	porosity factor $[\text{cm}^{-1}]$
Pr	Prandtl number $\left(\frac{\nu}{\alpha_T}\right)$
q	thermal flux $\left(\frac{\text{cal}}{\text{cm} \cdot \text{sec}}\right)$
q_l	thermal flux in liquid $\left(\frac{\text{cal}}{\text{cm} \cdot \text{sec}}\right)$
q_q	thermal flux in quartz $\left(\frac{\text{cal}}{\text{cm} \cdot \text{sec}}\right)$
Ra	combined Rayleigh number $(Ra_S + Ra_T)$
Ra_S	solutal Rayleigh number
Ra_T	thermal Rayleigh number
s	half distance between dendrite arms
t	time (sec)
t_s	local solidification time (sec)
T	temperature
T_0	reference temperature ($^{\circ}\text{C}$)
T_e	eutectic temperature ($^{\circ}\text{C}$)
T_m	melting temperature ($^{\circ}\text{C}$)
u_l	liquid velocity in the horizontal (x) direction $\left(\frac{\text{cm}}{\text{sec}}\right)$
u_s	solid velocity in the horizontal (x) direction $\left(\frac{\text{cm}}{\text{sec}}\right)$
u	effective liquid velocity $(\bar{u} = v_l \cdot g_l)$ in the horizontal (x) direction $\left(\frac{\text{cm}}{\text{sec}}\right)$
\bar{u}	average velocity $\left(\bar{u} = \frac{1}{\rho}(\bar{\rho}_l u_l + \bar{\rho}_s u_s)\right)$ in the horizontal (x) direction $\left(\frac{\text{cm}}{\text{sec}}\right)$
\hat{u}	pseudo velocity in the horizontal (x) direction $\left(\frac{\text{cm}}{\text{sec}}\right)$
v_l	liquid velocity in the vertical (y) direction $\left(\frac{\text{cm}}{\text{sec}}\right)$
v_s	solid velocity in the vertical (y) direction $\left(\frac{\text{cm}}{\text{sec}}\right)$
v	effective liquid velocity $(v = v_l \cdot g_l)$ in the vertical (y) direction $\left(\frac{\text{cm}}{\text{sec}}\right)$
\bar{v}	average velocity $\left(\bar{v} = \frac{1}{\rho}(\bar{\rho}_l v_l + \bar{\rho}_s v_s)\right)$ in the vertical (y) direction $\left(\frac{\text{cm}}{\text{sec}}\right)$
\hat{v}	pseudo-velocity in the vertical (y) direction $\left(\frac{\text{cm}}{\text{sec}}\right)$
\mathbf{V}_l	liquid velocity vector $\left(\frac{\text{cm}}{\text{sec}}\right)$
\mathbf{V}_s	solid velocity vector $\left(\frac{\text{cm}}{\text{sec}}\right)$
V	solidification velocity $\left(\frac{\text{cm}}{\text{sec}}\right)$
V_0	electric field $\left(\frac{\text{volts}}{\text{cm}}\right)$
$\bar{\mathbf{V}}$	average velocity vector $\left(\bar{\mathbf{V}} = \frac{1}{\rho}(\bar{\rho}_l \mathbf{v}_l + \bar{\rho}_s \mathbf{V}_s)\right)$ $\left(\frac{\text{cm}}{\text{sec}}\right)$

Greek Symbols

α_S	solutal diffusivity $\left(\frac{\text{cm}^2}{\text{sec}}\right)$
α_T	thermal diffusivity $\left(\frac{\text{cm}^2}{\text{sec}}\right)$
β_S	solutal coefficient of volumetric expansion $\left(\frac{1}{\text{wt}\%}\right)$

β_T	thermal coefficient of volumetric expansion ($\frac{1}{^\circ\text{C}}$)
Δx	horizontal distance between cell faces (cm)
Δy	vertical distance between cell faces (cm)
Δt	numerical time step interval (sec)
γ	surface energy ($\frac{\text{ergs}}{\text{cm}^2}$)
λ	wavelength of the laser light
ρ	average mass density of the mixture ($\frac{\text{gm}}{\text{cm}^3}$)
ρ_k	mass density of the k phase ($\frac{\text{gm}}{\text{cm}^3}$)
$\bar{\rho}_k$	partial mass density of the k phase ($\frac{\text{gm}}{\text{cm}^3}$)
ρ_0	mass density of reference bulk fluid ($\frac{\text{gm}}{\text{cm}^3}$)
ν	kinematic viscosity ($\frac{\text{cm}^2}{\text{sec}}$)
σ	temporal growth parameter ($\frac{1}{\text{sec}}$)
Ω	supersaturation ratio
Ψ	curve fit coefficient ($\frac{1}{\text{cm}}$)

Subscripts

b	bottom
c	critical value
eff	effective value
f	field varying
i	interface
l	liquid
q	quartz
s	solid
0	reference value